GEANT4 SIMULATIONS AND EXPERIMENTAL TESTS OF A SILICON CD DETECTOR

GEANT4 SIMULATIONS AND EXPERIMENTAL TESTS OF A SILICON CD DETECTOR

By

JUN CHEN, B. Sc.

A Thesis
Submitted to the School of Graduate Studies
in Partial Fulfilment of the Requirements
for the Degree
Master of Science

McMaster University

MASTER OF SCIENCE (2006) McMaster University
(Physics and Astronomy) Hamilton, Ontario

TITLE:	GEANT4 Simulations and Experimental Tests of A Silicon CD Detector
AUTHOR:	Jun Chen, B. Sc. Peking University Beijing, P. R. China, 2002
SUPERVISOR:	Dr. Alan Chen
NUMBER OF PAGES:	XII, 80

Abstract

In nuclear astrophysics, there are still undiscovered areas involving unstable nuclei, like the nucleosynthesis in exploding stars. The unstable nuclei are extremely difficult to produce in the laboratory for study since they decay away quickly once they are formed. To make the unstable nuclei available in the laboratory, Canada has built one of the best facilities in the world for nuclear astrophysics studies with radioactive beams, called TRIUMF-ISAC. Its recent upgrade to ISAC-2 can produce even heavier radioactive beams with higher energy. To fully utilize the ISAC-2 facility, a high-segmented HPGe γ-ray detector—TIGRESS, has been developed to study exotic nuclei using the well-established technique of Coulomb Excitation.

As an essential part of the TIGRESS facility, auxiliary detectors, such as silicon detectors, are used to improve the sensitivity of the experiments through Doppler correction. Two types of silicon detectors will be used. One is the CD-shaped double-sided silicon strip detector,which is the topic of this thesis. The other one is the silicon barrel detector. This thesis will discuss the computer simulations and experimental tests of the CD detector.

Simulations were made using a simulation toolkit GEANT4, which was run under the Linux system. The goal was to test the hypothesis that measurements of the energies of heavy ions in Coulomb excitation may improve the Doppler correction by constraining the scattering location in a thick target. To test the performance of the simulated CD detector, simple simulations were performed for

shooting calibration alpha particles from an ^{241}Am source first directly onto the CD and second through a thin target onto the CD. The goal of additional simulations was to attempt to determine the corresponding scattering depth in a thick target by putting an energy cut on the spectrum of the scattered beam detected in the CD. These simulation results verify the possibility of such localization, though the resolution is not very good.

Experimental tests for the CD detector are aimed to obtain the energy resolution for each strip element of the CD and to have at least 8 channels instrumented in our test lab before this detector is sent to TIGRESS facility. The test station including electronics and detector systems and all results from initial tests are described in detail in this thesis.

To my family.

Acknowledgments

First, I would like to thank my very nice supervisor Dr. Alan Chen, for his clear and patient guidance that directed me to fulfill this thesis. His valuable suggestions and feedback contributed greatly to this thesis.

I am grateful to Dr. Tom Drake, who gave me great help in using GEANT4. I greatly appreciate his coming to McMaster from Toronto to help me every time.

I also thank our technician Kenrick Chin, who taught me lots of experiment skills and helped me much in completing my experimental tests.

I would like to thank my other thesis committee member: Dr. Jim Waddington, who always was very nice and respectable. I also thank him for his instruction in nuclear physics.

I thank Anthony Olivieri, who helped me in setting up our test station last summer and I also thank the rest of our group: Chris and Lesley.

Last but not least, I thank my parents and my brother for supporting me all the time and thank my beloved wife who always gives me the greatest support in my life. I thank all the people who have given me help and support during my two years of study, especially my roommates: Zheping Huang, Xiaohan Wang and Xiang Huang.

Table of Contents

List of Figures

List of Tables

Chapter 1

Introduction

This thesis is about a silicon CD detector, which will be used as an auxiliary detector for the TRIUMF-TIGRESS spectrometer [1] at the ISAC-2 [2, 3] facility. In this chapter, I will give some introduction to these facilities. Before that, I will give some background to these facilities and to our research in nuclear astrophysics.

1.1 Nuclear Astrophysics

When you look into the sky dotted with countless shining stars, you might say "how the stars are shining". But, you might never think of these further: why the stars are shining, where do these stars come from, and furthermore, our universe and even human beings. In nature, all the matter is made from chemical elements, which are created through nuclear reactions occurring during the early evolution of our universe. To explore the evolution and structure of our universe, a new scientific field was developed, called nuclear astrophysics—the combination of astronomy and nuclear physics. Those nuclear processes responsible for the formation of the elements in our universe are collectively called "nucleosynthesis" [4]. One of the main goals of nuclear astrophysics is to study these nucleosynthesis pro-

cesses by measuring the properties of the nuclei that participate in them. These nucleosynthetic processes are discussed in the following sections.

1.1.1 Big Bang Nucleosynthesis

According to the big bang theory [5, 6, 7], our universe originated from a "big bang" cosmic explosion. During this Big Bang phase, the universe was very hot and dense, however, since then it has been expanding and cooling, allowing galaxies, stars, planets, and also the living beings on our earth to form. The primordial processes are known as Big Bang nucleosynthesis.

Big Bang nucleosynthesis (BBN) took place shortly after the Big Bang, and is responsible for the production of some light elements (mainly hydrogen, helium, and some lithium) [8, 9]. BBN has a very short life time, only about three minutes, after which the universe began to cool and expand, reducing the temperature and density. When the gravitational energy became larger than the thermal energy, the interstellar gas (mainly hydrogen and helium) condensed and this converted the gravitational energy to thermal energy and so the temperature rose again. If the temperature became high enough, nuclear reactions commenced with the ignition of the most easily burned nuclear fuel—hydrogen. Then the basic nucleosynthetic process of the hydrogen burning ensued.

1.1.2 Hydrogen Burning

In this nucleosynthetic process, hydrogen is burned and finally converted into helium. There are two different sets of reactions in this process—the proton-proton (p-p) chain and the CNO (carbon-nitrogen-oxygen) cycle.

The pp chain reactions

The proton-proton fusion reactions are the main reactions that take place when the Sun and other stars with the mass of our Sun or less burn [10, 11]. This reaction

chain includes two major steps.

The first step is the fusion of two hydrogen nuclei ^{1}H (protons) into deuterium ^{2}H, resulting in one proton changing into a neutron and the emission of a positron and a neutrino.

$$^1H + ^1H \rightarrow ^2H + e^+ + \nu_e$$

As this is a weak interaction, this first step is extremely slow allowing a proton to wait for a very long time before fusing into deuterium. But once the deuterium is formed, it quickly fuses with another hydrogen to produce a light isotope of helium, ^{3}He, and release a gamma-ray:

$$^2H + ^1H \rightarrow ^3He + \gamma$$

There are three main branches following this step, namely, the pp1, pp2 and pp3 chain reactions, all of which lead to the same end—generating the helium isotope ^{4}He.

CNO cycle

The CNO cycle is another fusion reaction sequence by which helium is produced from hydrogen [11]. This cycle begins with ^{12}C and ends with a return to ^{12}C, while converting four protons to produce one helium nucleus just like the p-p chain reactions described above. Here the carbon is simply a catalyst. The CNO cycle is shown in figure 1.1. In the N-Z plane, the cycle takes the form as shown in figure 1.2. At the even higher temperatures resulting from the energy released by the fusion reactions, proton capture on ^{13}N can begin to compete with its β-decay in the CNO cycle, leading to "break out" into the Hot CNO cycle. Figure 1.3 shows one Hot CNO cycle branch at temperature $^1T_9$=0.2. The Hot CNO cycles are the main source of energy generation in novae, and in the early stages of X-ray

[1]This is the denotation of temperature in astrophysics. $T_9 = 10^9$K, which means T_9=0.2 equivalent to T=0.2×10^9K.

bursts [12].

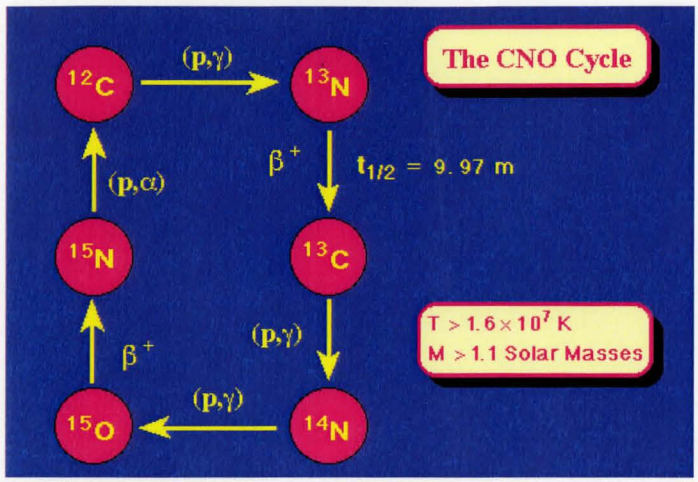

Figure 1.1: The CNO cycle [13].

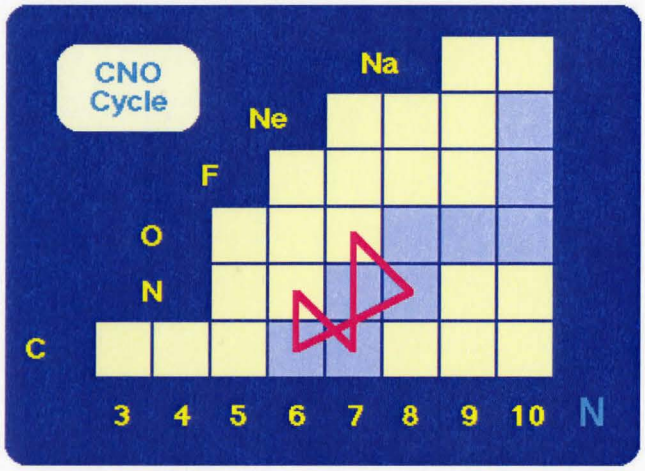

Figure 1.2: The CNO cycle in the plane of neutron number and proton number. This figure is adapted from [13].

1.1.3 Helium Burning

In the hydrogen burning phase, a balance between the thermal pressure and the gravitational force is established by the released energy, which stabilizes the star until the exhaustion of the hydrogen. Then the star contracts again causing grav-

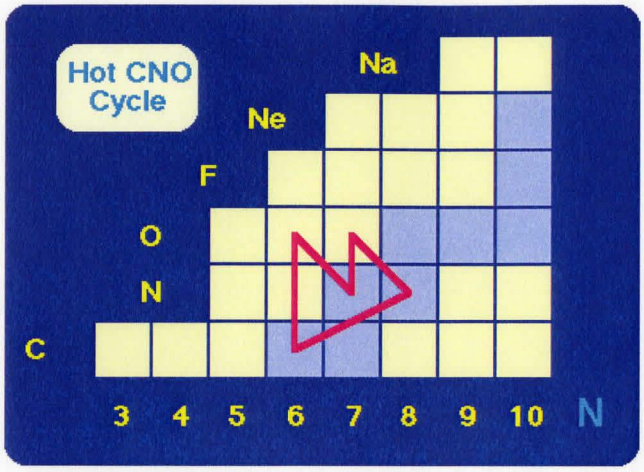

Figure 1.3: One Hot CNO cycle branch at T_9=0.2 in the plane of neutron number and proton number [13].

itational energy to be converted to thermal energy. The temperature and density keep increasing till the next available nuclear fuel, helium, begins to burn. In this burning process, three helium nuclei can fuse to form a carbon nucleus by the so-called triple-alpha process [14, 15].

$$^4He + ^4He + ^4He \rightarrow ^{12}C + \gamma$$

With the energy released from burning helium, the gravitational force is balanced again by the thermal pressure. Once the ^4He fuel is also exhausted, the star begins to cool down again and the gravitational collapse resumes. At some stage, the star then moves into its next phase.

1.1.4 Advanced and explosive Burning

The carbon burning phase starts when the temperature reachs a high level due to further gravitational collapse after helium burning. As carbon burns, heavier reaction products, such as O, Mg, Ne, are produced [16]. After the star runs out of carbon, the core again contracts until Neon ignition. During the neon burning phase, Oxygen and Magnesium are created [17]. As the star consumes all its neon

and the star contracts still further, its density and temperature keeps rising until oxygen burning becomes energetically possible. When the star finally consumes its oxygen, a new core rich in silicon comes into being [18, 19].

In further silicon burning, silicon nuclei are broken down into helium nuclei, which are then added into other silicon nuclei to produce the elements, namely, chromium, manganese, iron, cobalt, and nickel [20].

No more burning processes can happen after the silicon burning in a star's evolution, since its final product, ^{56}Fe, is very stable and iron burning is not energetically possible. Therefore, the star core keeps cooling down and the gravitational force is no longer balanced by thermal energy, so this leads to the collapse of the star. A supernova explosion may occur with a neutron star or a black hole coming into being. A huge amount of energy is released from such an explosion, making possible the production of elements beyond iron by other nucleosynthetic mechanisms, e.g. the rapid capture of neutrons (r-process).

1.1.5 Nucleosynthesis beyond Iron

Now it is well known that there are two types of evolutionary mechanisms [21], the s-process and the r-process, responsible for producing the heavier elements with the iron-peak nuclei as seeds. Both processes bypass the proton-rich nuclei along the valley of stability. But there are some proton-rich nuclei thought to be those from ^{74}Se to ^{196}Hg, which can not be produced by the two neutron-capture (r and s) processes and are believed to be produced by a third mechanism called p-process. Figure 1.4 shows the paths of the three processes in the plane of neutron and proton number.

The r-process

In a hot and neutron-rich environment, the radioactive nuclei can absorb neutrons very rapidly with the absorbing time shorter than their β-decay life-times.

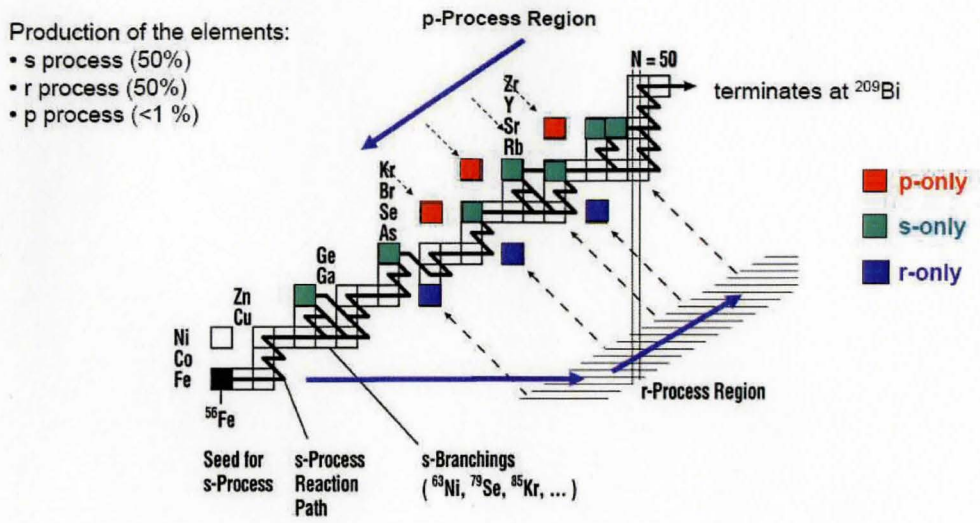

Figure 1.4: The paths of the r-,s- and p- processes in the plane of neutron and proton number.

Highly unstable neutron-rich nuclei are formed but then quickly β decay to stable ones. Such a nucleosynthetic process is called the "r-process". About half the elements heavier than iron on the neutron-rich side of the valley of stability have been produced through this process. Due to the high neutron density requirement (exceeding $\sim 10^{20}$ cm^{-3}), the r-process likely occurs in supernova explosions and neutron star mergers.

The s-process

The s-process is a slow neutron-capture process, relative to the β-decay. It takes place in an environment with lower neutron density and lower temperature. Stable isotopes are produced as the process moves along the valley of stability, while in the r-process nuclei are produced very far away from the valley of stability due to continuous neutron captures before their β-decays. The s-process produces nearly the same number of isotopes as the r-process does.

The p-process

The p-process includes two mechanisms of the nucleosynthesis of some rare heavy proton-rich nuclei. One is the photodisintegration of the product nuclei from the r-process and the s-process in a hot environment where photons obtain enough energy to remove neutrons or α-particles from the nuclei. A series of (γ,n) and (γ,α) reactions are involved in this mechanism; that is why the "p-process" is sometimes called the "γ-process". In a hot and proton-rich environment, proton-capture reactions become possible. When the temperature and proton density become extremely high, rapid proton-capture occurs, which is called "rp-process". Till today the cosmic site for the rp-process is still not firmly established like the s-process, but is believed to occur in X-ray bursts on accreting neutron stars.

1.2 The TIGRESS Spectrometer at ISAC

Nuclear processes in nucleosynthesis involving stable nuclei in pp-chains, CNO cycles have been well established, but those involving unstable nuclei—neutron-rich nuclei on the path of r-process and proton-rich nuclei on the path of rp-process in exploding stars— are still unclear(Figure 1.5). It is because unstable nuclei are very difficult to produce in the laboratory due to their extremely short life-times. To make unstable nuclei available, many facilities for nuclear astrophysics studies with radioactive ion beams (RIB) have been built worldwide. TRIUMF-ISAC [3], is one of them, which is located in Vancouver, Canada. With the TRIUMF-ISAC facility, we have been able to perform experiments with RIB and sophisticated detection systems, in some cases reproducing the actual nuclear processes that happen in the universe [22]. The recent upgrade of ISAC-1 to ISAC-2 [2] will make the ISAC facility more efficient for studies of very exotic nuclei using the technique of Coulomb excitation, for example. To fulfill this task, a γ-ray spectrometer, TIGRESS, has been developed and is now under construction.

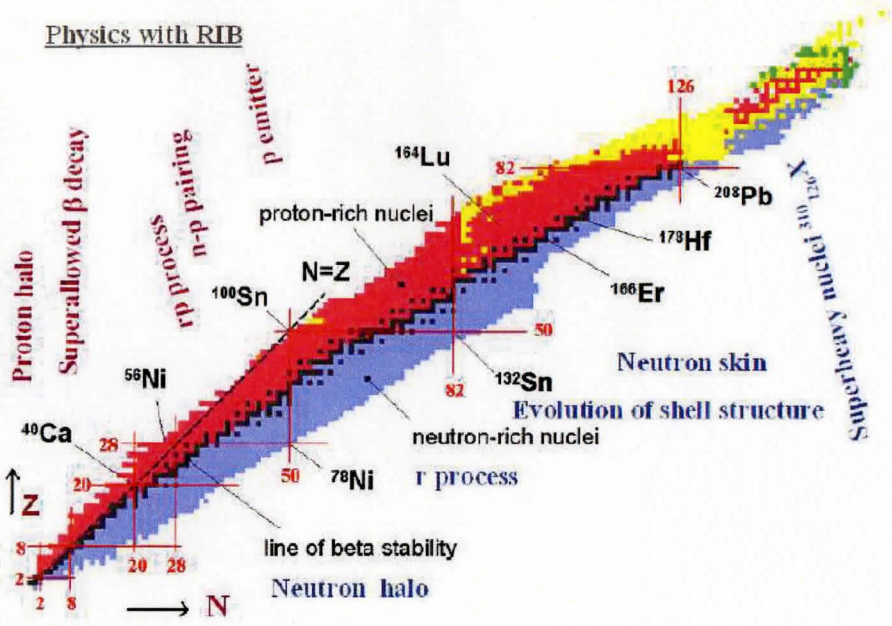

Figure 1.5: Physics with radioactive ion beam. This figure is from [23].

1.2.1 ISAC

ISAC—the isotope separator and accelerator, is one of the most advanced RIB facilities of the isotope separator on-line (ISOL) [22] type in the world. The RIB is produced by bombarding thick production targets with up to 100μA of 500MeV protons from TRIUMF's main cyclotron. Then the produced high-quality RIB can be delivered directly to a variety of experimental facilities, or can be re-accelerated to energies typical of explosive astrophysical events (~0.5-1.5MeV/A) [3]. Figure 1.6 is a schematic of the TRIUMF-ISAC facility.

The old version of ISAC, ISAC-1, can produce RIB with the mass number up to A=30 and energy up to 1.5MeV/A. Its upgrade version, ISAC-2, will be able to produce RIBs with the mass number extended to A=150 and the energy to 6.5MeV/A for the entire mass range and 15MeV/A for light nuclei [2]. Figure 1.7 shows a photograph of ISAC-2 experimental hall.

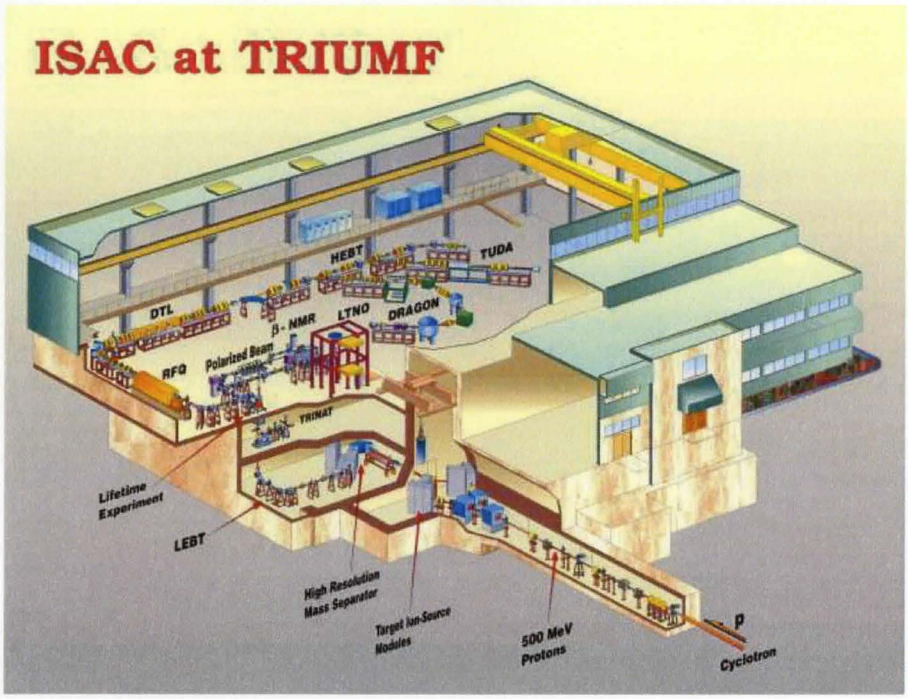

Figure 1.6: Schematic of the TRIUMF-ISAC facility.

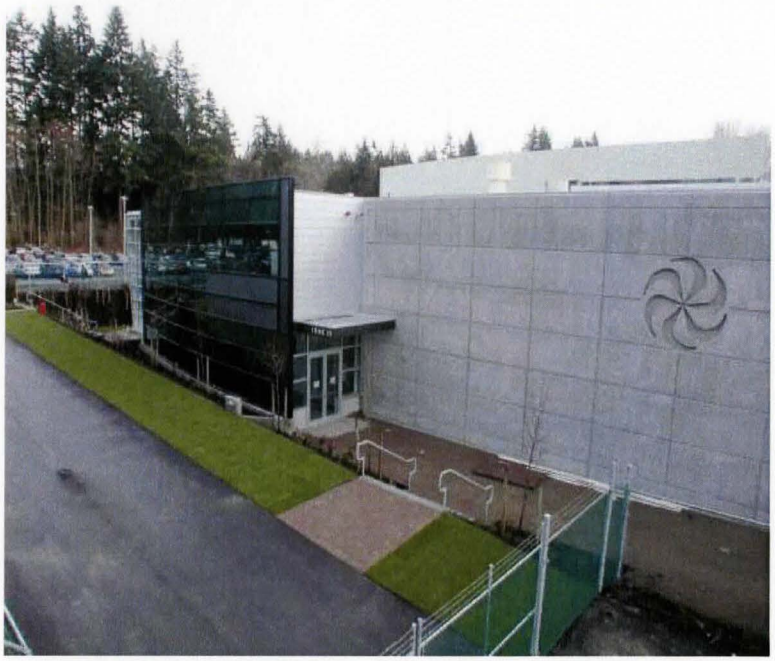

Figure 1.7: A photograph of the ISAC-2 experimental hall.

1.2.2 TIGRESS spectrometer

TIGRESS—(TRIUMF-ISAC Gamma-Ray Escape Suppressed Spectrometer) [1]—is designed to study the exotic nuclei from the ISAC facility, in particular ISAC-2. It is a highly segmented gamma-ray spectrometer which consists of 12 Compton-suppressed HPGe detectors in closed-packed geometry. TIGRESS can be used in the fields of nuclear astrophysics, nuclear structure, nuclear reactions, and fundamental interactions.

The early experiments with TIGRESS will be to measure quadrupole matrix elements using low-energy Coulomb excitation of RIBs. Auxiliary detectors will be necessary to detect, in coincidence with the γ-ray detection, the scattered beam particles and the target recoils as well. A silicon CD detector will be used at the early stages of these experiments. A silicon barrel detector will also be included in the future. Figure 1.8 shows the schematic of the TIGRESS spectrometer.

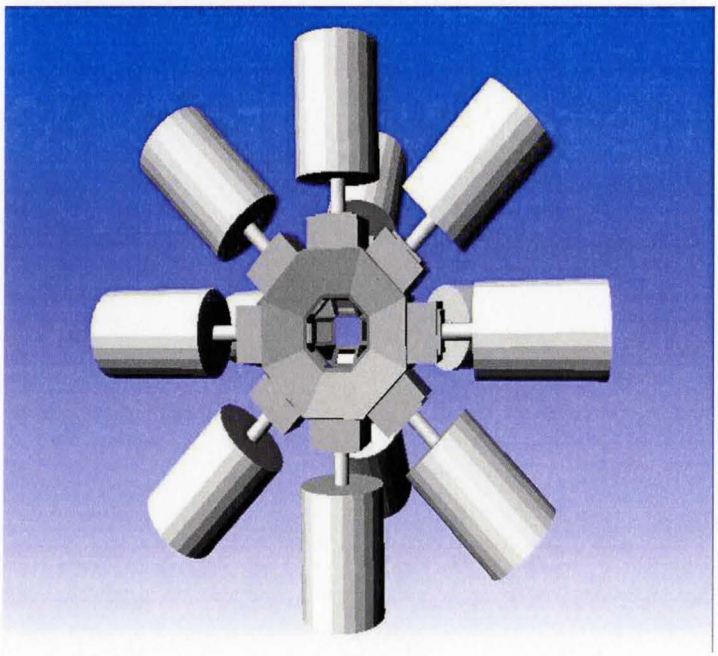

Figure 1.8: Schematic of the TIGRESS spectrometer.

1.2.3 Experimental Technique—Coulomb Excitation

Coulomb excitation (coulex) is a nuclear excitation of the target nucleus caused by the long-range Coulomb interaction between colliding nuclei. Coulex is an established technique which has been extensively used as a probe for studies of nuclear structure. The target nucleus to be studied is bombarded by heavy ions with kinetic energy below that needed to cause nuclear interaction. The beam or target nucleus can be excited to a higher energy level by the Coulomb interaction, and subsequently de-excite by emitting a gamma-ray. By detecting a coincidence of the γ-ray in the TIGRESS spectrometer and the scattered radioactive beams ion and/or the target recoil in large solid angle detectors, one can obtain information about nuclear structure, such as the energy of the excited states and the electromagnetic transition rates.

1.2.4 Auxiliary Detectors—Silicon Barrel detector and CD detector

For the Coulex studies with the TIGRESS facility, auxiliary detectors are indispensable for detection of scattered beam particles or target recoils in coincidence with gamma-ray detection. The sensitivity of the overall experiment and the accuracy of the results will get improved with the auxiliary detectors added in. The charged particle detector of good energy resolution, large solid angle coverage and highly compact geometry, will be fitted into the TIGRESS target chamber. The auxiliary silicon detector chosen consists of two components shown in figure 1.9. One is an annular double-sided silicon strip detector (CD detector) discussed in detail in this thesis, covering forward angles up to 40 degrees with respect to the beam direction; the other one is a silicon barrel detector array which surrounds the target and covers scattering angles from about 40 degrees to 137 degrees in the laboratory frame. The CD detector is used for small-angle scattering, particularly when the target particle is lighter than the beam particle, while the silicon

barrel detector array is important in measurements where the target particle is heavier than the beam particle and therefore scattering angles get much larger. Figure 1.10 shows the placement of the silicon CD detector within the TIGRESS target chamber.

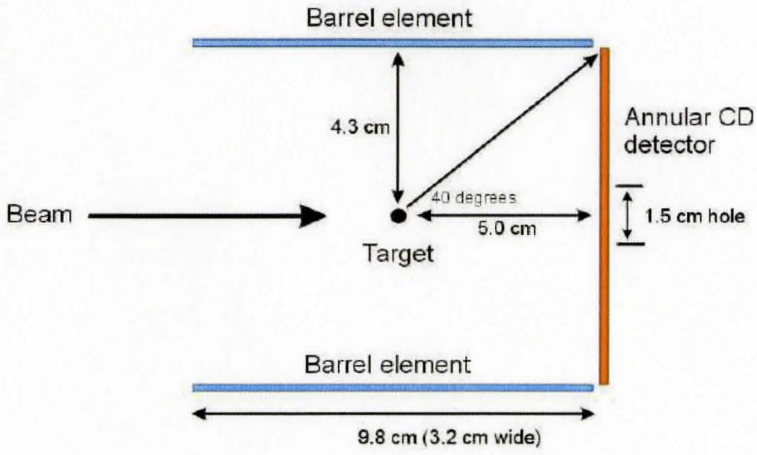

Figure 1.9: A schematic of the auxiliary silicon detector for TIGRESS.Two barrel detector elements and a CD detector are shown.

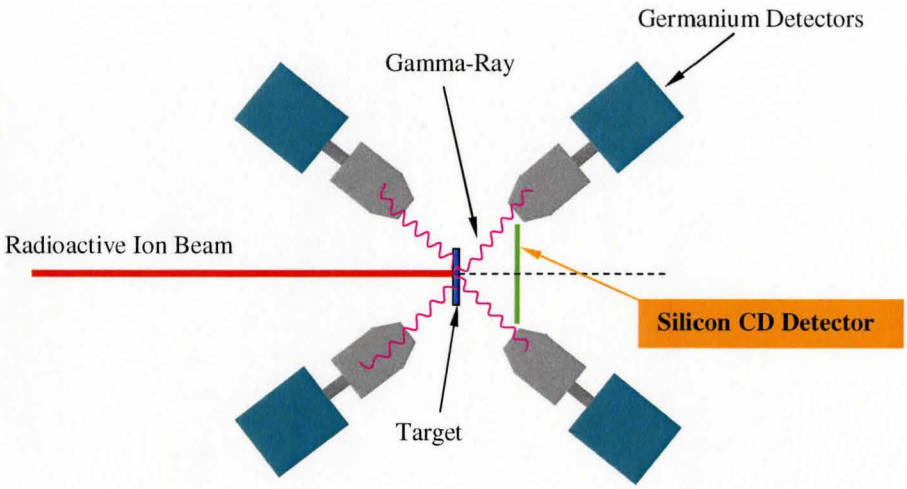

Figure 1.10: A schematic of TIGRESS showing the placement of the silicon CD detector whin the TIGRESS target chamber.

Chapter 2

Silicon CD Detectors

For charged particle detection, silicon is the most widely used semiconductor material. As has been noted, future TIGRESS experiments will use a silicon CD detector to measure the energy and position of the scattered radioactive beam particle and target recoil. In this chapter, I will briefly review the theory of semiconductor detectors [24] and then describe the silicon CD detector.

2.1 Theory of Semiconductor Detectors

The semiconductor detectors, also called "solid-state detectors", are made of crystalline semiconductor materials, usually silicon or germanium. This kind of detector is used extensively in nuclear physics and high energy physics. Silicon is used in the diode detectors for charged particle detection, e.g. the CD detector [25], which is discussed in this chapter, whereas Germanium is more widely used in detectors for gamma-ray detection, e.g. the TRIUMF-TIGRESS spectrometer [1]. More details about germanium detectors can be found in reference [26].

2.1.1 Energy Band Structure in Solids

In solids the periodic lattice structure of crystalline materials creates a periodic potential, which results in two energy bands for all electrons in the solids — the conduction band and valence band [27]. The energy bands are actually regions of many closely spaced energy levels. The valence band is composed of the lower energy levels in which the electrons are tightly bound and not free to move, whereas in the conduction band composed of the higher energy levels, the electrons have enough energy to become free from bound states and therefore can move through the entire crystal. These electrons in the conduction band contribute to the electrical conductivity of the material. Between the two energy bands, depending on the types of the materials in the solids, there may exist a region in which there are no confined electrons and which is thus given a name "forbidden" energy gap. The figure 2.1 shows the energy band configurations of three different solids for comparison – insulators, semiconductors and conductors.

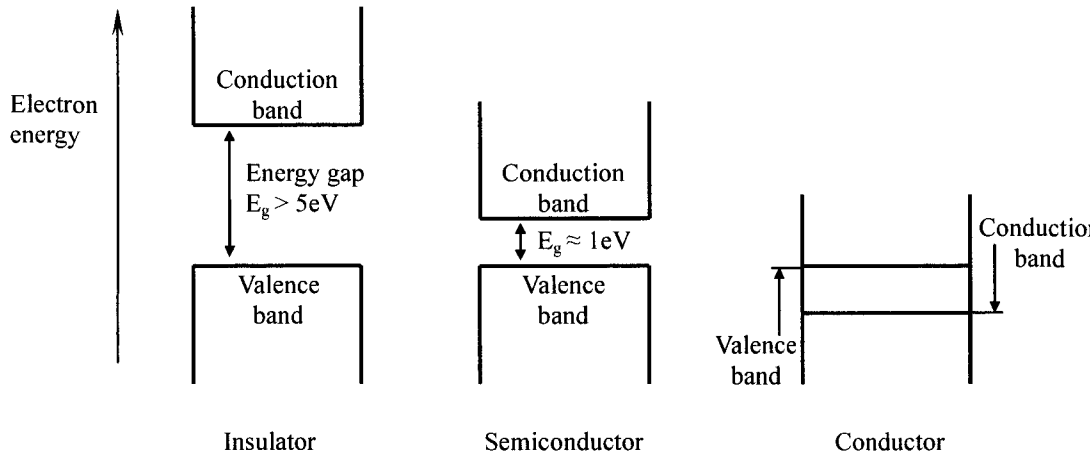

Figure 2.1: Energy band structure of insulators, semiconductors and conductors

In insulators and semiconductors, the forbidden energy gap exists and all the electrons lie in the valence band at room temperature. So the materials do not show electric conductivity until the electrons in the valence band can obtain enough external energy to jump across the energy gap into the conduction band. For

insulators, the energy gap, or the energy required to jump across the gap, is 5 eV or more, whereas for semiconductors, the gap is much smaller, about 1 eV. In conductors, however, the valence band and conduction band overlap, that is no energy gap, and the electrons in the valence band can easily migrate to the conduction band.

2.1.2 Charge Carriers in Semiconductors

The forbidden energy gap between the valence band and the conduction band in semiconductors is very small,as we know from above, only 1 eV for Si and 0.67 eV for Ge. At room temperature, therefore, only by intrinsic thermal excitation some electrons in the valence band can be excited into the higher energy level in the conduction band and become free electrons, leaving vacancies (called "holes") in the original position of each electron. If an external electric field is applied, the free electrons in the conduction band can move to conduct the electric current. At the same time, their corresponding holes will move in directions opposite to those of the electrons. So the holes act like a positive charge carrier and also conduct the electric current. There are thus two kinds of charge carriers in semiconductors — free electrons in the conduction band and holes in the valence band, whereas in conductors only electrons act as charge carriers.

In pure semiconductor crystals the number of holes in the valence band is the same as that of the electrons in the conduction band. However, in practical applications, a small amount of impurity atoms is doped into the crystal to improve the efficiency of the production of the charge carriers. Usually a pentavalent dopant is used to provide extra electrons in the conduction band, and a trivalent dopant is used to provide extra holes in the valence band. Semiconductor materials with the former dopant have the negative electrons as the majority charge carriers and are thus called n-type semiconductors, whereas those with the latter dopant have the positive holes as majority charge carries and are thus called p-type semiconductors. If heavily doped, the two types of semiconductors will be called n^+-type

semiconductors and p^+-type semiconductors, respectively.

2.1.3 The p-n Semiconductor Junction

If a n-type semiconductor and a p-type semiconductor are pressed together, a so-called p-n junction will be formed, on which all present semiconductor detectors are based. In practical fabrication, the p-n junction is made by diffusing p-type impurities into one end of an n-type semiconductor to change that end into p-type.

Because of excess of electrons in the n-type end and holes in the p-type end, there is an initial diffusion of electrons towards the p-side and holes towards the n-side during the formation of the junction. This is illustrated in figure 2.2. This diffusion makes negative electrons and positive holes accumulate on the initial electric neutral p-side and n-side respectively, which establishes an intrinsic electric field across the junction with the direction from the n-side to p-side. This electric field prevents the charge carriers from further diffusing, leaving a region associated with the electric field, of immobile space charges, called "depletion region". Any electron entering the depletion region will be swept towards the n-side by the electric field and any hole similarly will be swept towards the p-side. This is just the property of the p-n junction that is used for the detection of radiation.

2.1.4 Ionizing Radiation of Charged Particles in the p-n Junction

When passing through semiconductors, charged particles lose energies through interactions with the electrons in the semiconductors. Although some other processes also occur simultaneously, they contribute much less to the energy loss and can thus be ignored [26]. In these interactions, energy is transferred from the charged particle to the electron, promoting it to the conduction band to produce an electron-hole pair. Such a process is called ionization. As we have seen, a semiconductor has a very small forbidden energy gap. To create an electron-hole pair

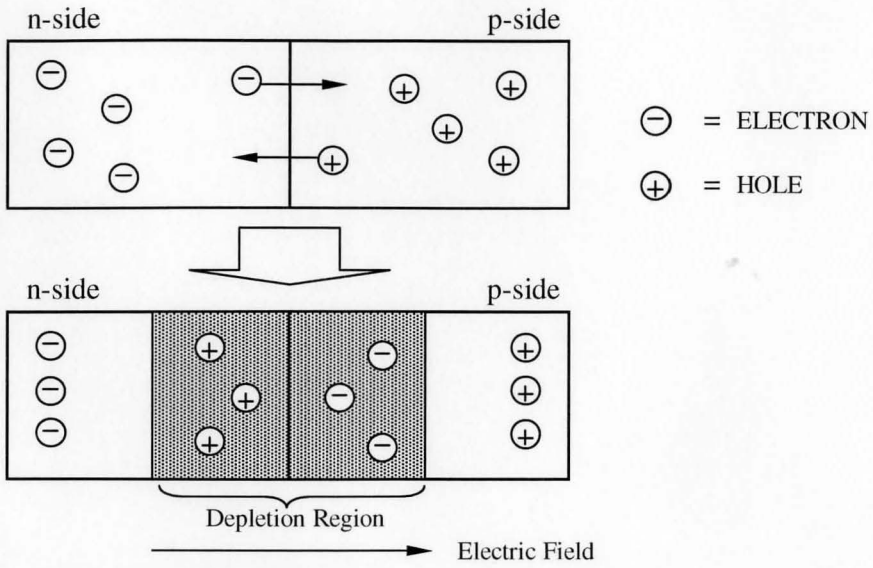

Figure 2.2: The formation of p-n junction by carriers diffusion

in Si, only an average energy, denoted by ε, of about 3 eV is required, compared with about 30 eV in typical inert gas-filled ionization detectors.

2.1.5 Semiconductor Diode Detectors and Reverse Biasing

If the total energy loss of incident charged particles in a p-n junction is denoted by ΔE, then the total number of electron-hole pairs produced is:

$$number\ of\ electron - hole\ pairs = \Delta E/\varepsilon$$

where ε is the average energy required to produce an electron-hole pairs. These electrons and holes are then swept out by the electric field in the depletion region of the p-n junction and accumulate on the n-side and p-side respectively. Through a charge-sensitive preamplifier, a signal can be brought out from each side of the junction.

The key aspect of a semiconductor diode detector is the depletion region whose width is proportional to the strength of the electric field in it. In general, the intrinsic electric field caused by the initial diffusion of charge carriers is not in-

tense enough to provide efficient charge collection and therefore an external bias is needed. If a forward bias is applied to the p-n diode junction, from p-side to n-side, obviously the intrinsic electric field of the depletion region will be canceled resulting in the disappearance of energy gap, and thus the p-n junction becomes a conductor. On the contrary, if a reversed bias is applied, the potential between the two sides of the n-p junction will increase, broadening the width of the depletion region and thus the sensitive volume for charge collection will increase. The higher the external bias voltage, the wider the depletion region and the more efficient the charge collection. Of course, there exists a voltage limit dependent on the resistance of the diode junction beyond which the junction will breakdown and become conductive. Figure 2.3 shows the Bias Voltage vs. Current properties of a diode.

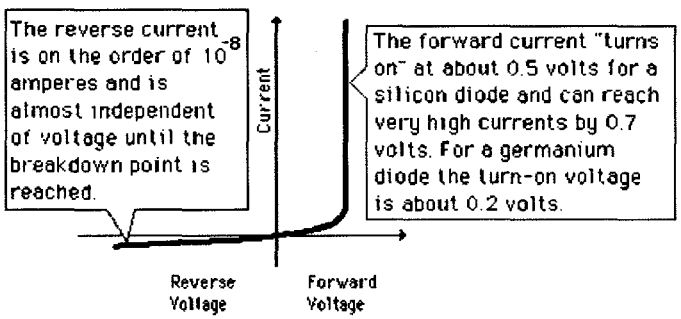

Figure 2.3: Current vs Voltage characteristics of p-n Junction

2.1.6 Silicon Micro-Strip Detectors for Position Detection

In experiments of nuclear physics, the measurement of the energy of the charged particles after interaction alone is not enough. Position sensitivity is also required. To this end, two types of silicon position-sensitive detectors were developed. One is the continuous position-sensitive detector [26]. The other is the silicon micro-strip detector, which is more widely used today. The CD detector discussed in this thesis is also based on the silicon micro-strip detector.

The micro-strip detector is actually a discrete array of many silicon micro-strip

elements. Each micro-strip element has its own readout, through which a signal can be taken when the incoming particle hits this strip, and its position information is then determined by the location of the strip. In the next section, the possibility of more accurate position determination is discussed with a double-sided silicon strip detector.

2.2 Compact Disc Double Sided Silicon Strip Detector

The silicon CD detector is a double-sided silicon strip detector array. It was designed by the Edinburgh-Louvain collaboration [25] for Coulomb Excitation and charged-particle reactions with radioactive beams. The detector can be fabricated small enough to fit inside a large solid angle γ-detector, e.g. TIGRESS spectrometer [1] at TRIUMF and serve as an auxiliary detector. More details about this detector are given below and the instrumentation for this detector system is described in Chapter 4.

2.2.1 Description of the CD Detector

The CD detector has a size and shape similar to a real music CD and thus gets its current name. It has active outer and inner diameters of 84 mm and 16 mm respectively and consists of four quadrants. Figure 2.4 shows its schematic structure. Each quadrant of the detector has 16 annular strips of 1.9 mm width and 2 mm pitch on the front side and 24 sector strips of 3.4° pitch on the back side, which results in 40 discrete detector elements and total 160 elements for the whole detector. Therefore, it can provide a very close compact geometry in the target region with a horizontal and azimuthal angular resolution at a distance of 5 cm away from the target of $\Delta\Theta \sim 2°$, $\Delta\Phi \sim 3.4°$ respectively.

The actual CD detector, as shown in figure 2.5, is a little different from what

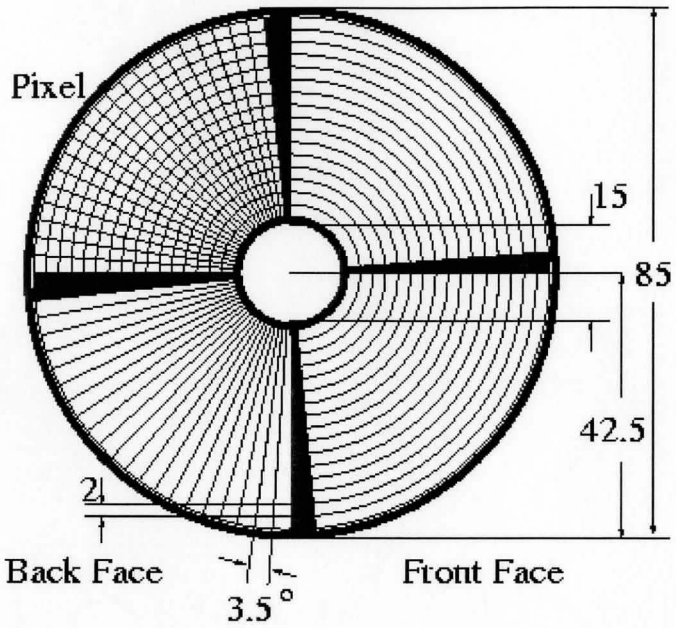

Figure 2.4: Schematic structure of CD detector (dimensions in mm) [25]. The two right-hand quadrants show the schematic layout of the front side of the detector, the lower left-hand quadrant shows the layout of the back side, and the upper left-hand shows the quasi-pixels formed by the overlap of front annular strips and back sector strips.

is described above. The azimuthal angular coverage for each quadrant is reduced down to 82° from 90° to leave necessary space for the signal PCB tracks of the annular strips on the front face of the detector, as can been seen on the top of figure 2.5.

The silicon wafer of the detector can be made with different thicknesses for different uses. A thin CD detector can be used as particle identification detector when combined with a following residual detector [25]. The CD detector used in our program will serve as an end detector and thus has a considerable thickness of about 400 μm so as to stop the incident charged particles in the detector.

Figure 2.6 shows the cross-section of the detector. The detector is fabricated using an ion-implantation method. When fabricated, annular strips of p^+-type silicon are directly implanted on one side of an n-type silicon bulk and sector strips of n^+-type silicon are implanted on the other side. The implantation depth

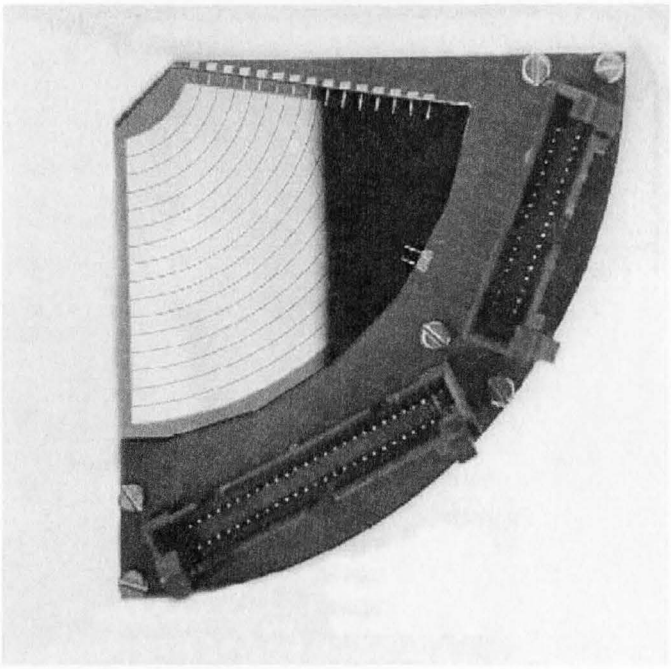

Figure 2.5: Photograph of a mounted CD detector quadrant showing the p^+ junction side of the device.

for both sides is 0.4-0.5 μm. On the top of each strip, an aluminum contact of 0.2-0.3 μm thickness is plated. The neighboring aluminum contacts are isolated by an insulating SiO_2 gap with the same thickness as the contacts.

2.2.2 Detection Mechanism of the CD detector

As mentioned in the last section, a strip detector can measure the energy deposited in the detector, as well as the position of the incident particles on it. But for an one-sided silicon strip detector, we can only obtain 1D information, that is, we can just tell which strip the incident particles hit and do not know the particular position on that strip. Then we can imagine that since a one-sided detector can provide 1D information, a double-sided detector will be able to give 2D information. That is why we use the double-sided silicon strip detector (DSSSD). When particles shoot onto the detector, two coincident signals are produced: one from one strip on one side and the other from the orthogonal strip on the other side. These give the

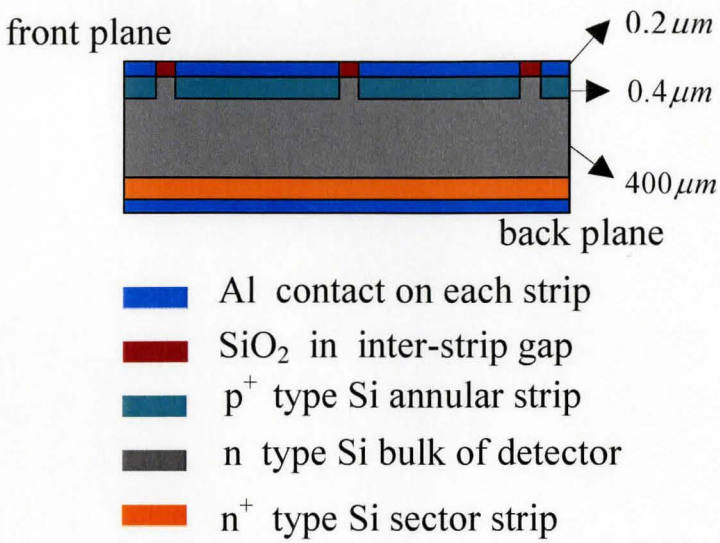

Figure 2.6: Cross-Section of CD detector. It just shows the details for the front face. The back face has the same structure.

particle position for a single event in the detector. We have used a rectangular detector an end detector for the DRAGON facility [28, 29] at TRIUMF and the ISOLDE facility [30] at CERN. Our CD detector is designed to provide closer compact geometry.

Experimental tests for the silicon CD detector are described in Chapter 4. In the next chapter, a simulation toolkit used to simulate the CD detector is introduced followed by a discussion on the simulations for the CD detector.

Chapter 3

GEANT4 Simulations

Before performing experimental tests for the CD detector in our laboratory, I carried out some computer simulations for the CD, with the goal of locating the collision spot for scattering in a thick target from the residual energy of the beam particles detected in the CD. The specific software for this task is the so-called *GEANT4* package, a very powerful new object-oriented simulation toolkit [31]. In this chapter, a detailed introduction to this software is given, followed by one of the topics of this thesis—the simulations of the CD detector in GEANT4.

3.1 The GEANT4 Toolkit

GEANT4 is a software package used to simulate the interactions when particles pass through matter. It is used extensively in many research fields, such as particle physics, nuclear physics, accelerator design, space engineering and medical physics. In fact, wherever particles interact the GEANT4 toolkit can be used for simulations.

3.1.1 Introduction

GEANT4 was designed and developed so as to meet the ever-increasing demand for large-scale, accurate and comprehensive simulations of the particle detectors used in modern particle and nuclear physics. It is based on an abundant set of physics models, which come from the accumulated experience of many contributors to the field of Monte Carlo simulation of particle detectors and physical processes, to handle the interactions between incident particles and matter for a wide energy range, from ~250 eV to ~1 TeV.

A GEANT4 simulation process usually includes the following aspects:

1. the geometry of the system
2. the materials involved
3. the fundamental particles of interest
4. time generation of primary particles for events
5. the tracking of particles through materials and external electromagnetic fields
6. the physics processes governing particle interactions
7. the response of sensitive detector components
8. the generation of event data
9. the storage of events and tracks
10. the visualization of the detector and particle trajectories
11. the capture for subsequent analysis of simulation data at different levels of detail and refinement

To cover these aspects, there exist 17 class categories[1] in GEANT4. The categories and their relations are shown in figure 3.1 [31]. Each box in the figure represents a class category, and the straight line with an open circle represents a usage relationship: the category at the circle end uses the adjoining category. The organization of the GEANT4 source codes follows basically the structure of this class category.

In the following, we describe some of the main GEANT4 units in the diagram in figure 3.1.

Run is the largest unit of simulation in GEANT4. One Run represents performing the simulation once. It consists of a sequence of events. Conceptually, a run is a collection of events which share the same detector conditions. Within a run, users can not change the detector geometry and settings of physical processes. In other words, the detector is inaccessible during a run.

Event is the main unit of simulation. An event represents the whole process of an incident particle from its emission from the particle gun, through interactions with the target particles if applicable, to coming to rest in or leaving the detector system. The number of events is set before each run.

Track is a snapshot of a particle. It represents a temporary state of a particle at an instance within an event and includes information for position and physical quantities of the current state of the particle. An event consists of thousands of tracks.

Step is "delta" information from the track of a particle. The information includes energy loss in the step, time of flight during the step, etc.

The GEANT4 toolkit is designed using the C++ language and adopts object-oriented methodology.

[1] In the object-oriented analysis and design methodology by Grady Booch [32], class categories are used to create logical units.

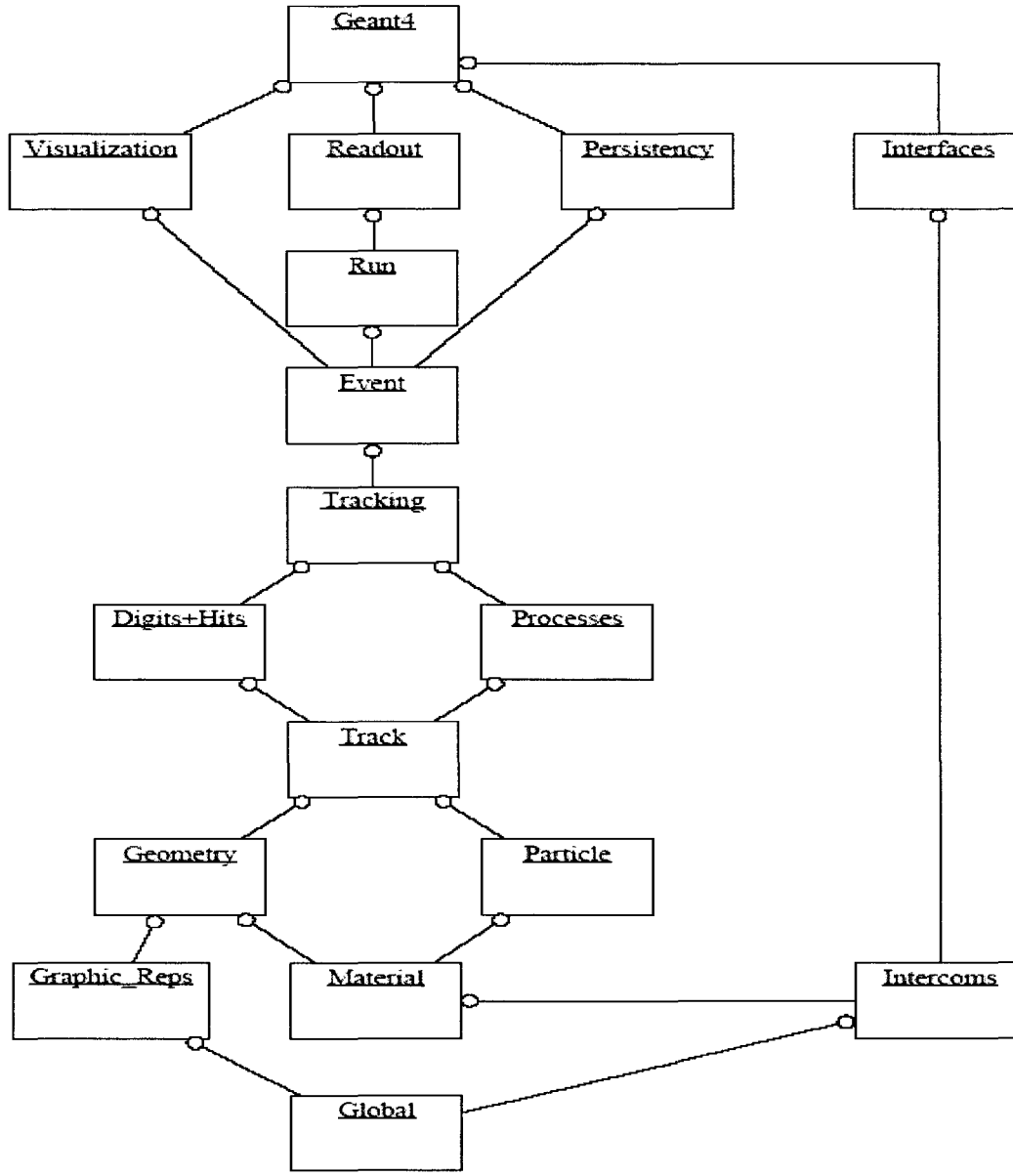

Figure 3.1: Class category diagram designed for GEANT4.

3.1.2 Using GEANT4

When making a simulation using GEANT4, the user does not need to care about the details of every aspect shown above. The toolkit can take care of most of them. What the user needs to do is just to construct the geometry of his/her own

detector system, and then add the necessary physical processes and finally set up the simulation conditions.

Figure 3.2 is the flow process diagram showing how GEANT4 works.

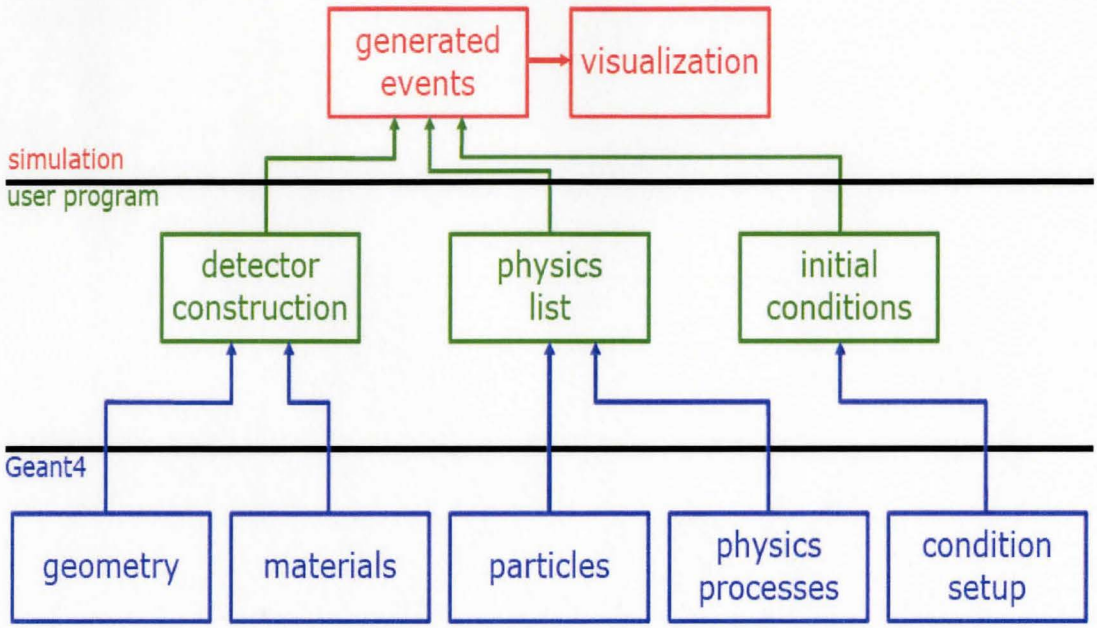

Figure 3.2: Flow process diagram of GEANT4

From the diagram, all that users need to do is in the user program: constructing the geometry of the system and defining the materials needed in the "detector construction" part; adding the relevant particles and physics processes in the "physics list" part; defining the user's actions and setting up the initial conditions in the "initial conditions" part. A simple example is given in the next section.

Fundamentals about some key components of GEANT4, like defining the geometry and materials, are described in the Appendix.

3.1.3 A Simple Example Using GEANT4 Toolkit

In this section, a simulation of geantino transportation[2] is constructed according to the diagram in figure 3.2. From that diagram, there are three steps in making a simulation:

Detector Construction

In the source file for detector construction, a tracker tube made of material Al and used to measure the coordinates of the incoming beam particles, and a calorimeter block made of material Pb and used to measure the energy of the incoming beam particles are constructed, using G4Tub and G4Box classes respectively.

Physics List

In the source file for the physics list, the particle which should be defined is only the geantino, and the relevant physics process is only transportation.

Condition Setup

In this simple example, we do not need to define any user's actions and we just set up the "particle gun" with desired energy, position and direction.

After finishing all of these, we can run the simulation and get the results of every event shown in figure 3.3:

[2]geantinos are virtual particles created in GEANT4 for simulation which do not interact with materials and undertake transportation processes only, in which no interaction happens between the particles and matter and thus no energy loss when particle is passing through matter, just like the particles are traveling in the vacuum.

****

* G4Track Information: Particle = geantino, Track ID = 1, Parent ID = 0

****

Step#	X(mm)	Y(mm)	Z(mm)	KinE(MeV)	dE(MeV)	StepLeng	TrackLeng	NextVolume	ProcName
0	-2.00E+03	0	0	1.00E+03	0	0	0	expHall	initStep
1	-1.60E+03	0	40	1.00E+03	0	402	402	tracker	Transportation
2	-400	0	160	1.00E+03	0	1.21E+03	1.61E+03	expHall	Transportation
3	0	0	200	1.00E+03	0	402	2.01E+03	caloBlock	Transportation
4	90	0	209	1.00E+03	0	90.4	2.10E+03	caloLayer	Transportation
5	110	0	211	1.00E+03	0	20.1	2.12E+03	caloBlock	Transportation
6	190	0	219	1.00E+03	0	80.4	2.20E+03	caloLayer	Transportation
7	210	0	221	1.00E+03	0	20.1	2.22E+03	caloBlock	Transportation
8	290	0	229	1.00E+03	0	80.4	2.30E+03	caloLayer	Transportation
9	310	0	231	1.00E+03	0	20.1	2.32E+03	caloBlock	Transportation
10	390	0	239	1.00E+03	0	80.4	2.40E+03	caloLayer	Transportation
11	410	0	241	1.00E+03	0	20.1	2.42E+03	caloBlock	Transportation
12	490	0	249	1.00E+03	0	80.4	2.50E+03	caloLayer	Transportation
13	510	0	251	1.00E+03	0	20.1	2.52E+03	caloBlock	Transportation
14	590	0	259	1.00E+03	0	80.4	2.60E+03	caloLayer	Transportation
15	610	0	261	1.00E+03	0	20.1	2.62E+03	caloBlock	Transportation
16	690	0	269	1.00E+03	0	80.4	2.70E+03	caloLayer	Transportation
17	710	0	271	1.00E+03	0	20.1	2.72E+03	caloBlock	Transportation
.....	.....	.....	.....	.....	.....				

Figure 3.3: Display of the results in GEANT4 simulations

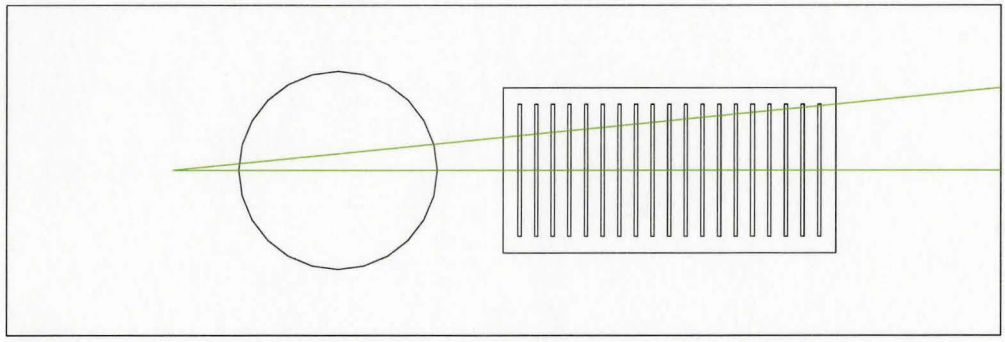

Figure 3.4: Visualization of geantinos transporting through a tracker tube and a calorimeter block.

3.2 GEANT4 Simulations for the CD Detector

This thesis is mainly about the simulations of the CD detector in GEANT4. The task of the simulations is to test the performance of the CD detector on the computer to get the information such as energy resolution of the detector, position sensitivity, etc. The details for all of these computer simulations are described in this section.

3.2.1 Geometry of the CD Detector in Geant4

The geometry of the CD detector was constructed according to the information in Ref. [25], as has been described in Chapter 2. Similarly to the fabrication process of the detector, the n-type silicon wafer with thickness 400 μm is constructed first, then the strips of thickness 0.4 μm together with their 0.2 μm aluminium contacts on top of them are constructed and placed on the top and bottom inside of the wafer, which is like the implantation process, and what is constructed afterwards are the inter-strip regions of SiO_2 with the same thickness as the aluminium contacts and they are placed in the region between strips. See this structure in figure 2.6 in Chapter 2. Figure 3.5 shows the visualization of the geometry of the CD detector in GEANT4.

3.2.2 The Simulation of Shooting Alpha Particles Directly onto the CD

The first simulation produced an energy spectrum using alpha particles impinging directly onto the CD detector at different angles. The particles considered in this simulation are only alpha particles, and the relevant physics process responsible for energy loss of the beam particles in the CD is electron ionization. The other process involved is the multiple scattering. These are all the information that needs to be included in the *physics list* part of the user's program.

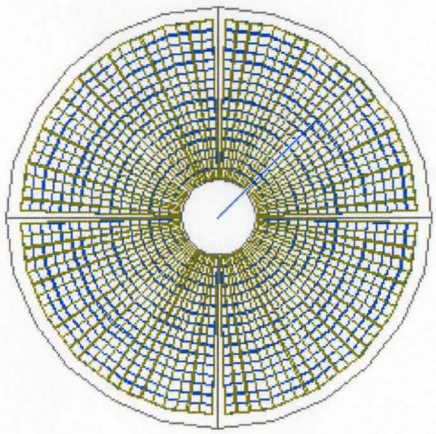

Figure 3.5: Visualization of the geometry of the CD detector in GEANT4

In order to simulate the performance of the real detector precisely, the energy loss in the aluminium contacts should be subtracted from the alpha energies since this part of energy loss does not contribute to electron-hole pair creation inside the depletion region of the detector element, which requires a sensitive detector volume to be chosen. The sensitive volume of a detector is the volume inside the detector responsible to count the energy deposit for energy measurement. The sensitive volumes of the CD detector are the silicon wafer and the heavily doped silicon strips on both sides of the detector. This is set in the *user-action* programs.

The particle gun for the alpha beam is set in the *PrimaryGeneration* program, with alpha particles from the most common calibration source ^{241}Am which emits alpha particles of energy 5.486 MeV (abundance: 85.2%) and 5.443 MeV (abundance: 12.8%). The particle gun is set to point towards the CD at a fixed angle, and its distance to the detector is 5 cm. Figure 3.6 is the visualization of the simulation obtained by the DAWNFILE visualization driver [31]. The angle of 15.8 degrees is just an arbitrary angle chosen for the visualization. The direction

of incident particles can be easily changed in the settings for the particle gun. Figure 3.7 illustrates the alpha spectrum from the results of this simulation.

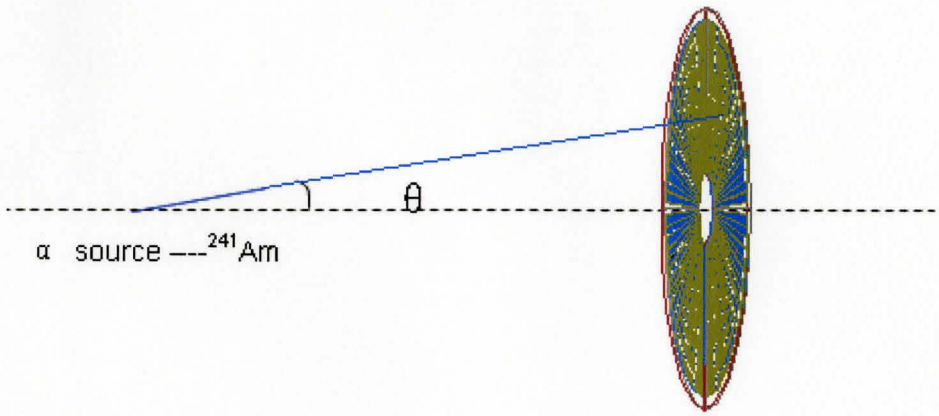

Figure 3.6: Visualization of alpha particles shooting onto the CD detector

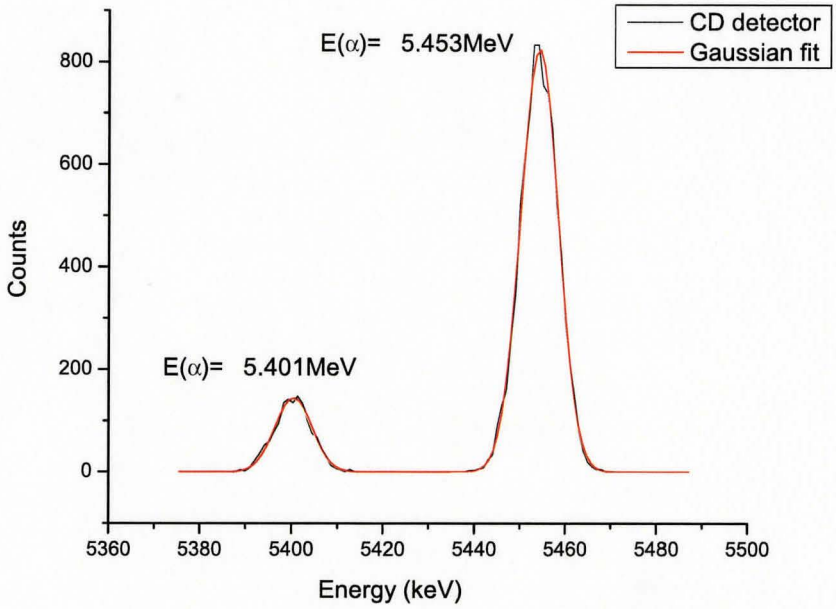

Figure 3.7: Alpha energy spectrum from the simulation results

To get the spectrum of the alpha particles from ^{241}Am, the simulation was run twice, because during each run the particle gun can shoot only one kind of particle with one specific energy. So I ran twice with the different particle guns with only the energy different, and with the total number of events for each run chosen according to the respective abundance, and then combined the two groups of results from the two runs into one. The energies of alpha particles in the spectrum are a little smaller than the initial energies of incident alpha particles, because the particles lost some energy in the aluminium contacts, with the magnitude of about 30 keV. But we can still see from the spectrum that the energy resolution is very high, about 11 keV (FWHM) for both $E(\alpha) = 5.401$ MeV and $E(\alpha) = 5.453$ MeV.

3.2.3 The Simulation of Shooting Alpha Particles onto a Thin Target

On the basis of the first simulation, a thin target(1 μg/cm^2 ^{12}C foil) was added to simulate alpha particles with energy of 5.486 MeV shooting onto the target and the residual energy of the particles was detected in the CD detector at different angles and to get an angular distribution of energy for the incident particles. The target was a disk with diameter of 3 cm, and its distance from the alpha source was 3 cm. Figure 3.8 is the visualization of this simulation in GEANT4.

For one run of the simulation, I obtained one result for a fixed angle, and then I changed the direction of the particle to get the result for another angle. I repeated this process and got the residual energies for different angles. Figure 3.9 illustrates the angular distribution of residual energy from these results.

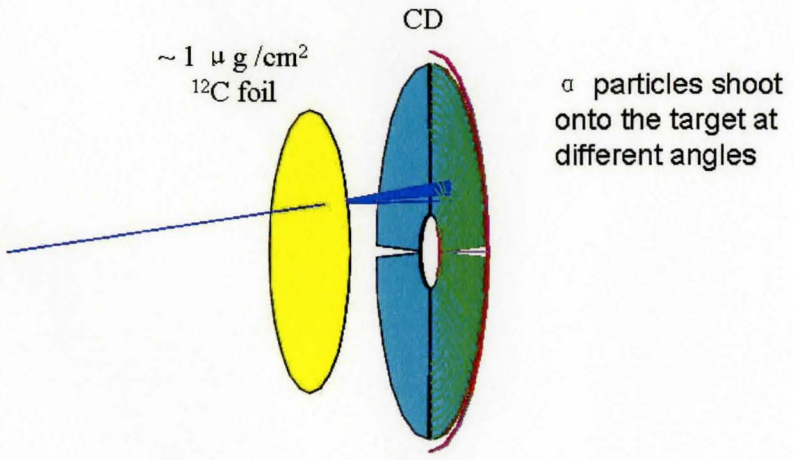

Figure 3.8: Visualization of alpha particles shooting onto a thin target

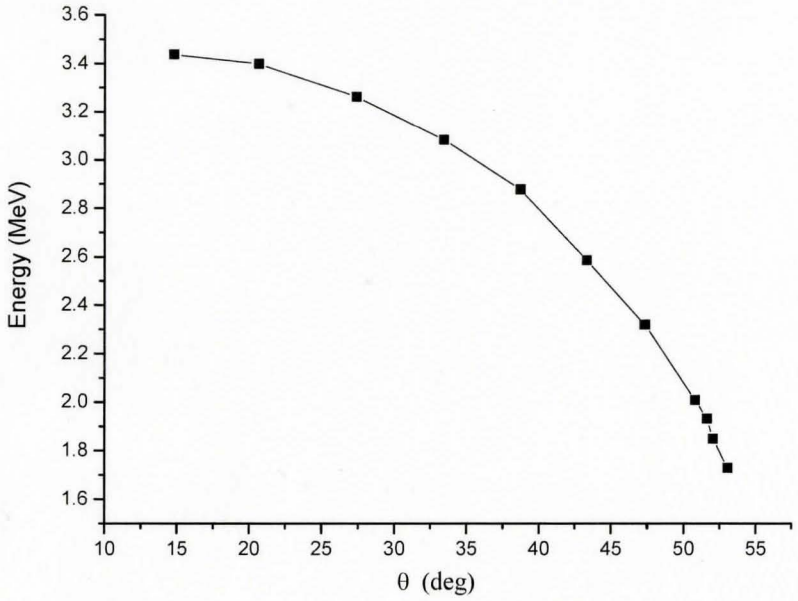

Figure 3.9: Angular distribution of α energy detected in the CD

3.2.4 Discussion for the First Two Simple Simulations

In the first simulation, the position information of the measured particles on the CD detector can also be easily obtained to determine which strips the particles hit. The angular distribution of energy in the second simulation shows that the residual energy detected on the CD detector decreases as the incident angle increases. That is because the path length of the incident particle through the target becomes longer as the incident angle increases, which causes more energy loss in the target. Figure 3.10 is the illustration of shooting alpha particles at different angles. So there should be a correlation between the path length through the target and the energy of particles detected in the CD detector.

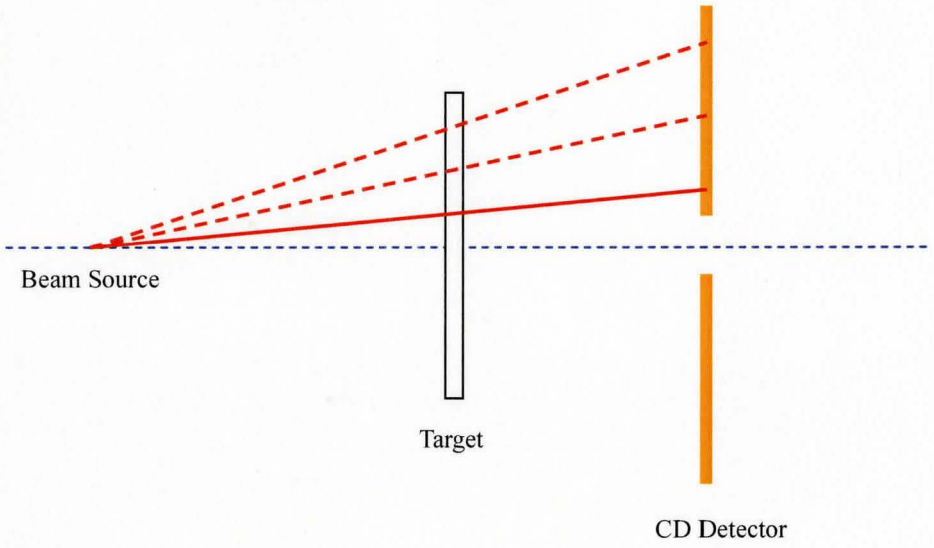

Figure 3.10: Illustration of shooting beam particles onto a thin target at different angles. The particles passed the target straightly and no scattering happening in the target is assumed.

In the above situation, it was assumed that there was no scattering happening and the incident particles just passed straight through the target and lost energy. This situation is similar to the scattering situation shown in figure 3.11, in which the incident particles are shot along the horizontal axis onto the thin target, and then at the front face of the target they are scattered into different angles. Combining this with the simulation results above, one can say the scattering angle and

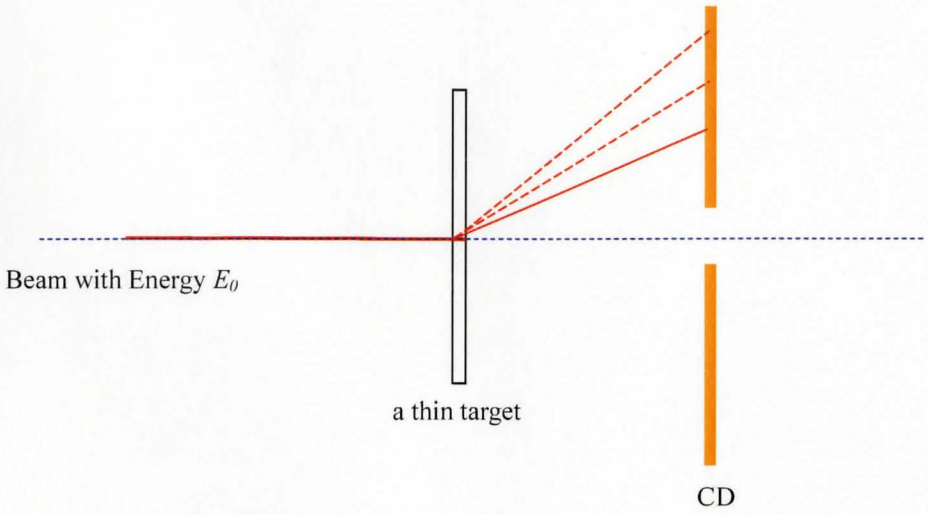

Figure 3.11: Illustration of beam particles impinging onto a thin target along the horizontal axis and scattered into different angles. It is similar to the situation in figure 3.10.

the residual energy in the CD have an one-to-one correlation. However, in a real situation, beam particles observed at a specific angle can be scattered from any point along the horizontal axis inside the target, not just at the beginning. Considering a very thin target, one can find that it almost makes no difference where the scattering takes place along the horizontal axis inside the thin target for a specific angle and the difference between their path lengths through the target can be ignored. This is shown in figure 3.12. Then, how about for the thick target? Things are different. For scattering taking place at different points along the axis inside the target, the path length of the incident particle through the target is different because the thickness of the target is considerable. Therefore, the total energy loss for different scattering position is different. Consequently, instead of getting one energy for each different angle as in the simulation for the thin target, apparently for the thick target one should get an energy distribution of the scattered particles detected in the CD detector for one angle and different energies in this distribution correspond to different scattering positions, or depth in the target. Then, we can hypothesize that if we find out the correlation between the

corresponding scattering depth in the target and the detected energy on the CD for a fixed angle, we can localize the scattering position through this correlation just by detecting the residual energy of the beam particles on the CD detector, which can provide information for Doppler correction of the gamma-ray energy resolution of the TIGRESS facility [1].

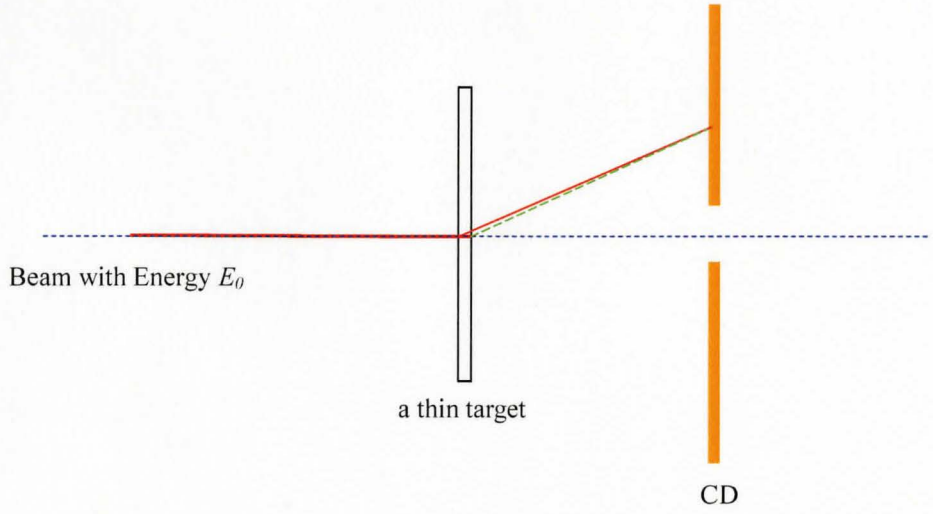

Figure 3.12: Illustration of beam particles scattered at the beginning (represented by the red solid line) and the end (represented by the green dashed line) of the target thickness at a same angle. Their energy losses can be considered as equal because the difference between their path length through the thin target can be ignored.

When γ-rays are emitted from moving nuclei and observed by a stationary detector, they will undergo a Doppler shift causing a relative frequency shift and consequently a spread in measured energy, which is called Doppler broadening. To correct this broadening, according to the equation below, θ must be determined, which is the angle between the emission direction of the γ-ray and the original direction of propagation of the radiating nucleus, and the velocity of the scattered beam must be determined as well as possible. This requires an accurate measurement of the origin of the γ-ray. That is, the scattering position should be determined as well as possible. The energy spread ΔE_γ caused by Doppler broadening effects for an γ-ray detector at angle θ is given by

$$\Delta E_\gamma = E_\gamma \beta \sin\theta \Delta\theta \tag{3.1}$$

where $\beta = v/c$ is the ratio of the velocity of the scattered beam to the speed of light and $\Delta\theta$ is the opening angle of the detector.

The illustration of different scattering depths is shown in figure 3.13

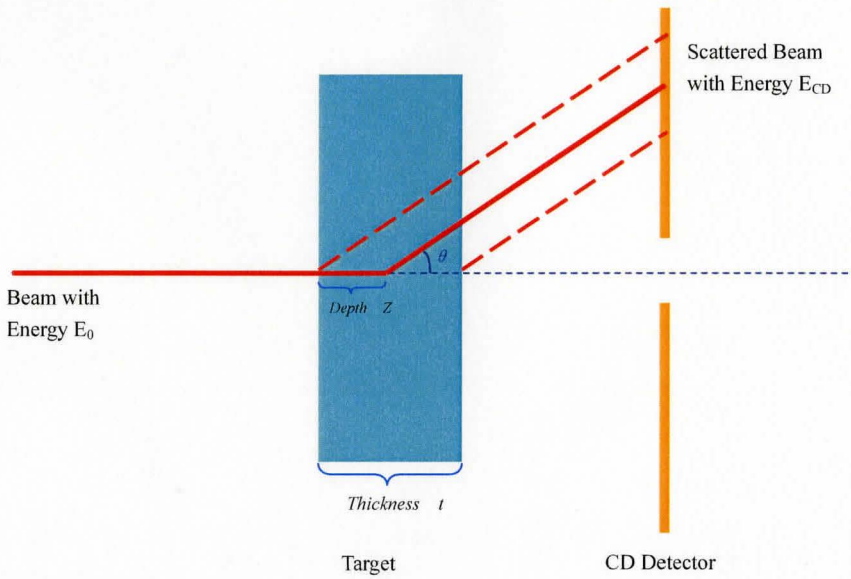

Figure 3.13: Illustration of shooting beam particles onto a thick target, with scattering at different angles (not to scale).

From the figure above, one can easily find the correlation of the elastic scattering depth Z with the detected energy E_{CD}, in terms of the target thickness t, the initial energy of the beam particle E_0, the specific scattering angle θ and the stopping power S of the target material. The correlation is written as in the form below[3]:

$$Z = \frac{cos\theta}{(1 - cos\theta) \cdot S} \cdot (E_{CD} - E_0) + \frac{t}{1 - cos\theta} \tag{3.2}$$

where the stopping power S is assumed to be constant and can be obtained by

[3]The results are just for an ideal situation: elastic scattering from an infinitely heavy target nucleus, that is with no energy transfer through the elastic scattering. However, in reality, we must consider inverse kinematics and the results will be different. Here we just discuss the ideal results to simply explain the localization technique.

deriving it from this equation:

$$S = \frac{cos\theta}{t + (cos\theta - 1) \cdot Z} \cdot (E_0 - E_{CD}) \tag{3.3}$$

To determine the stopping power S and verify the correlation, a SRIM [33] calculation was used. In the calculation, ^{110}Sn ions were chosen as the beam particles with the initial energy of $E_0 = 330$ MeV and the ^{58}Ni was chosen as the target with the thickness of $t = 2$ μm. Then an investigation was made for the particles scattered into the angle of $\Theta = 20°$, and the E_{CD} for different depths Z was calculated in SRIM simulation, such as $Z = 0$ μm, 1 μm, 2 μm. Figure 3.14 is the histogram of the simulations for the three depths. In the SRIM calculations for the E_{CD}, actually the depth values were not used directly. Instead, simulations were firstly made for the path length of the incident particle through the target up to each scattering depth, and simulations were then performed for the incident particle impinging normally onto a target with the thickness equal to the remaining path length for each depth after scattering. The remaining energy after this target of those incident particles which traverse this target without deflection is just the E_{CD}. But unavoidably, deflection happened for some particles due to multiple scattering and consequently the particles emerging from the target have a spread in energy. That is why an energy distribution was obtained instead of a single energy value. And the E_{CD} should be the peak value of the distribution. So, from the distribution, one obtains,

$$E_{CD} = 241 \text{ MeV, for } Z = 0 \ \mu\text{m};$$
$$E_{CD} = 245 \text{ MeV, for } Z = 1 \ \mu\text{m};$$
$$E_{CD} = 247 \text{ MeV, for } Z = 2 \ \mu\text{m};$$

Then one can calculate the stopping power using equation 3.3,

$$S = 41.8 \text{ MeV}/\mu\text{m, for } Z = 0 \ \mu\text{m};$$
$$S = 41.2 \text{ MeV}/\mu\text{m, for } Z = 1 \ \mu\text{m};$$
$$S = 41.5 \text{ MeV}/\mu\text{m, for } Z = 2 \ \mu\text{m};$$

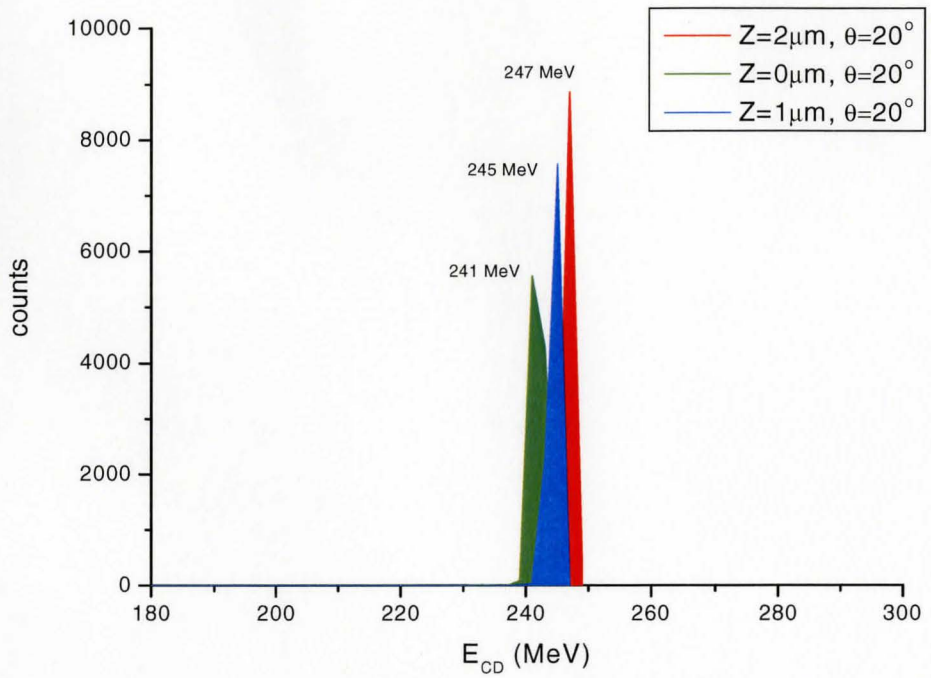

Figure 3.14: Histograms of E_{CD} for different depth Z in SRIM simulations

The Z-E_{CD} correlation using these S values are plotted in figure 3.15.

Calculating the stopping power for ^{110}Sn in the ^{58}Ni target directly with SRIM, gives,

$$S = 41.5 MeV/\mu m$$

which is consistent with the results calculated from the correlation within the uncertainty range of SRIM software—6% [34] and this result verifies the correlation between Z and E_{CD} to some extent.

3.2.5 Locating the Scattering Position with the Al-Sphere Detector

In the last section, we noted that by measuring the energy of the scattered particle detected in the CD detector, one can potentially locate where in the target the scattering has taken place, through a correlation between the energy and the penetration depth of the particle in the target material before scattering. Such a

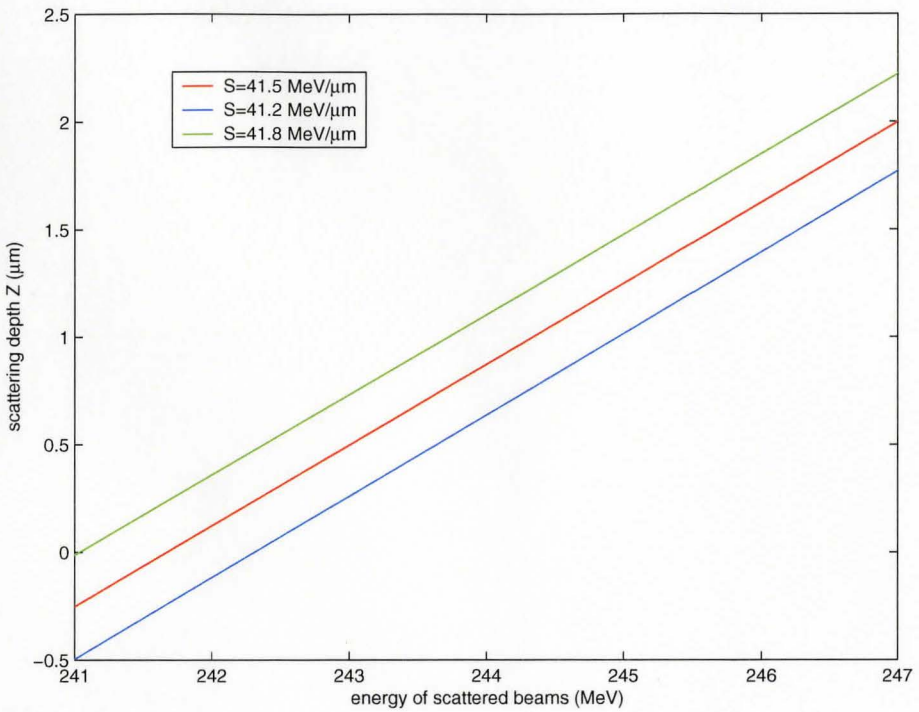

Figure 3.15: Correlation between Z depth in target and E_{CD} detected in the CD detector.

localization of interaction depth in the target can be used for Doppler correction of the γ-ray detected in TIGRESS. A further investigation was made using GEANT4. For simplicity, a simple Al-sphere detector was used for simulations instead of the CD detector.

The Al-sphere is a virtual detector just used for simulations. The CD detector can only cover the scattering angles from 10 degrees to 40 degrees with the detector 5 cm from the target while the sphere detector can cover all angles: the sphere shape is a simpler structure and is isotropic. These aspects make the Al-sphere detector ideal for simulations of scattering localization.

Figure 3.16 shows the geometry of this detection system in GEANT4.

In the case of 330 MeV ^{110}Sn impinging onto a 2 μm ^{58}Ni target, the physical process involved is elastic scattering. Figure 3.17 shows the simulation results. The energy spectrum in the above figure is the whole energy distribution for all

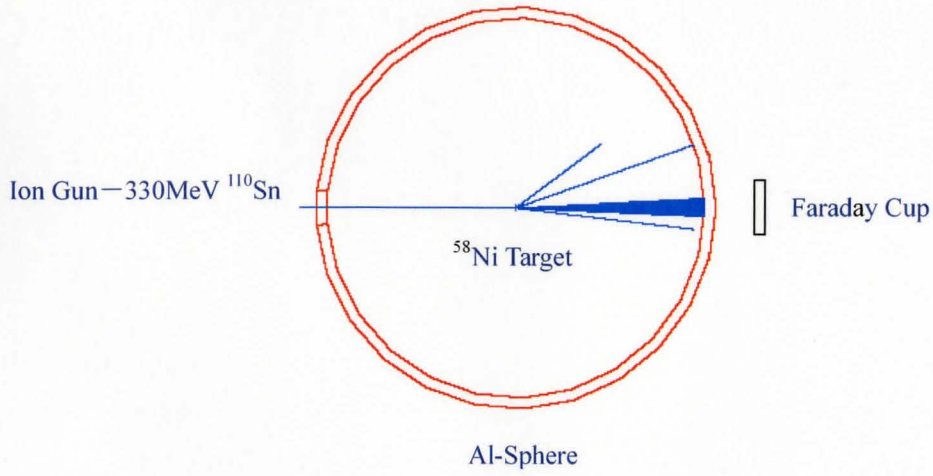

Figure 3.16: Visualization of simulations with Al-sphere detector in GEANT4.

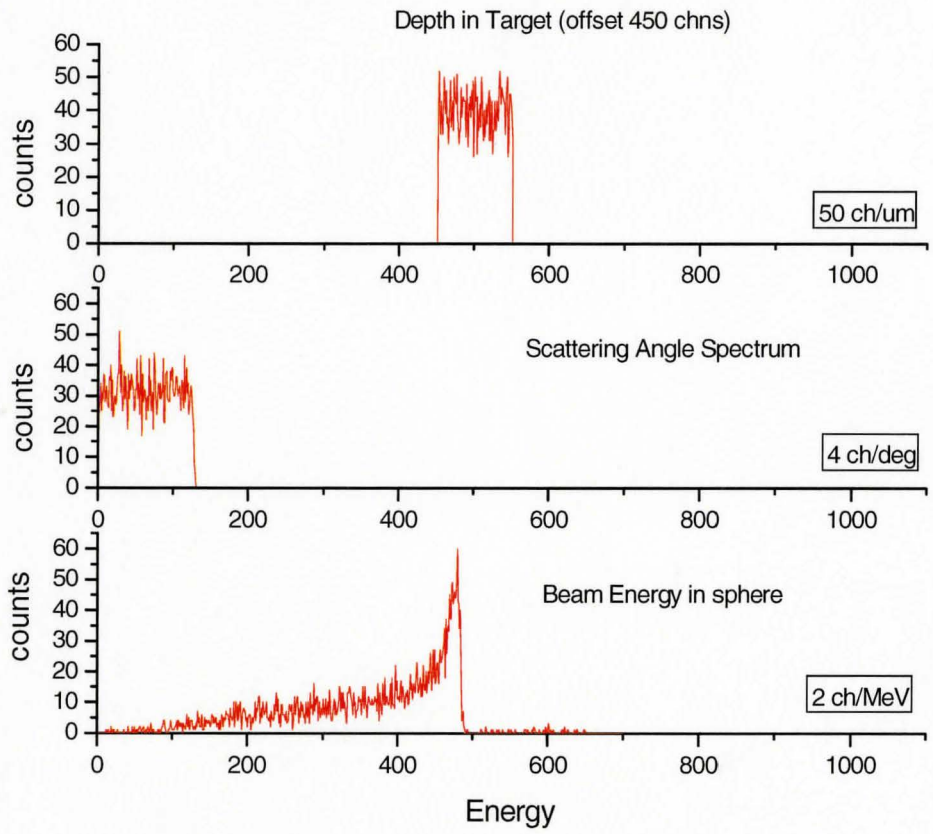

Figure 3.17: Spectra for depth in target,scattering angle and beam energy detected in Al-sphere.

scattering angles. By specifying an angle, one can obtain an energy spectrum for this angle. This energy spectrum should correspond to the whole range of the scattering depths in the target given by the correlation discussed in the last section. Therefore, by placing an energy cut on this specified energy spectrum, one should get a narrow depth distribution corresponding to this energy cut. And if a different energy cut is placed on the same energy spectrum, ideally one should get a completely separate depth distribution from the former one. Neighboring energy cuts should have neighboring depth distributions. Figure 3.18 and figure 3.19 illustrate this ideal situation. The two line-shaded rectangles in the top graph of the figure represent two energy cuts on the energy spectrum for a specified scattering angle. The bottom graph shows the corresponding depth distributions. However, the actual results from the simulations cannot reach this ideal level. Figures 3.20- 3.23 illustrate the actual situation in the simulations. The figures are explained in the following.

Each figure includes three spectra. The spectrum for a given parameter is determined by the other two parameters. The three parameters are : detected energy in the Al sphere detector – E_{sph}, scattering angle – Th_proj, and depth in target – Z_proj. The top one is the energy spectrum of detected ions in the Al sphere detector, which is thus determined by the parameters Th_proj and Z_proj. The middle one is the spectrum of scattering angle Th_proj, which is thus determined by the parameters E_{sph} and Z_proj. The bottom one is the spectrum of depth in target Z_proj, which is subject to the parameters E_{sph} and Th_proj. For the results in all of these figures, the three parameters were set in the following way: parameter Z_proj is always set through the whole range of the target thickness, parameter Th_proj is fixed to an arbitrary range of chosen angles — 20-21 degrees (channel 40-42), and only the cut on E_{sph} is changed to obtain all the spectra. With these settings, the top spectrum shows the distribution of all possible energies when the scattering angle is 20-21 degrees, the middle one shows the distribution of all the possible scattering angles corresponding to the specific energy E_{sph} cut set in each

energy graph and the bottom one shows the distribution of scattering depth corresponding to events in the E_{sph} cut, when the scattering events are observed at an angle in the range of 20-21 degrees. Every time the E_{sph} cut is changed, that selects an energy range in the top spectrum, and the corresponding distribution of possible scattering depths *Z_proj* is created in the bottom spectrum. An offset— 40 channels — is set only in this spectrum and the full target thickness indicated in the spectrum is thus from the 40th channel to the 60th channel.

The following list gives the calibrations of all the horizontal axes of the graphs in figures 3.20- 3.23. The total number of events in the simulations is set to 0.5 billion.

Top spectrum:	2.5 MeV per channel
Middle spectrum:	0.5 degree per channel
Bottom spectrum:	0.1 micron per channel

From these graphs, we can see that every different energy cut surely corresponds to a different depth distribution, and also, the peak of the distribution moves considerably as the energy cut changes. It seems at first sight that one can use these results for scattering location analysis and therefore use them as good reference datasets for Doppler correction. However,we found in the figure 3.24 below that the depth distribution covers the whole range of the target thickness. This shows a problem: for a specified energy cut, one cannot definitely tell at which spot or in which portion of the target thickness *Z_proj* the scattering takes place. One can only say that any position along the *Z_proj* is possible and only the probability of each position differs. This is not very helpful for Doppler correction. What we need for this correction is a definite scattering position, or at least a small range of the position within the whole range of the target thickness. It would be more useful if, corresponding to a specific energy cut, the depth distribution did not cover the whole range of the target thickness, because then at least one can exclude some target regions for scattered ions with the specific energy.

In these graphs, it seems that the depth distribution is more useful when the

energy cut is placed far away from the peak value of the energy spectrum, for example when the energy cut is set as channel 54-55 or channel 60-61. But in fact the reason why the depth distribution looks like that is that, as the energy cut is set farther and farther away from the peak value, the number of events corresponding to the energy cut will become fewer and fewer, which therefore causes the number of events in the depth distribution to decrease as well, resulting in even no counts in some region of less probable scattering depths. Actually, we found that increasing the number of incident particles will make the counts reappear in that region. Anyway, the depth distribution from the simulations always covers the whole range of the target thickness, no matter what scattering angle is specified, no matter what energy cut is chosen. This problem was also found in the simulations with a 4 μm target. What we can find useful from the results of the simulations is the probability of each possible scattering depth for a specific energy cut, by which together with statistical analysis some useful information can still be gathered for Doppler correction.

There might be a possibility that this problem is caused by the different energy losses of the scattered ions during the elastic collisions with the target ions. That is, for a specific scattering angle, although the peak position of the distribution is the most possible scattering spot, at other spots along the depth of the target thickness, the beam ions might transfer different energies to the target ions during the collision but at last combined with the different energy loss caused by ionization, the scattered ions may still have the same remaining energy as the most possible ones. But such events have less possibility and the farther away from the peak, the less the possibility is. That might be why the position distribution looks like what our simulations show.

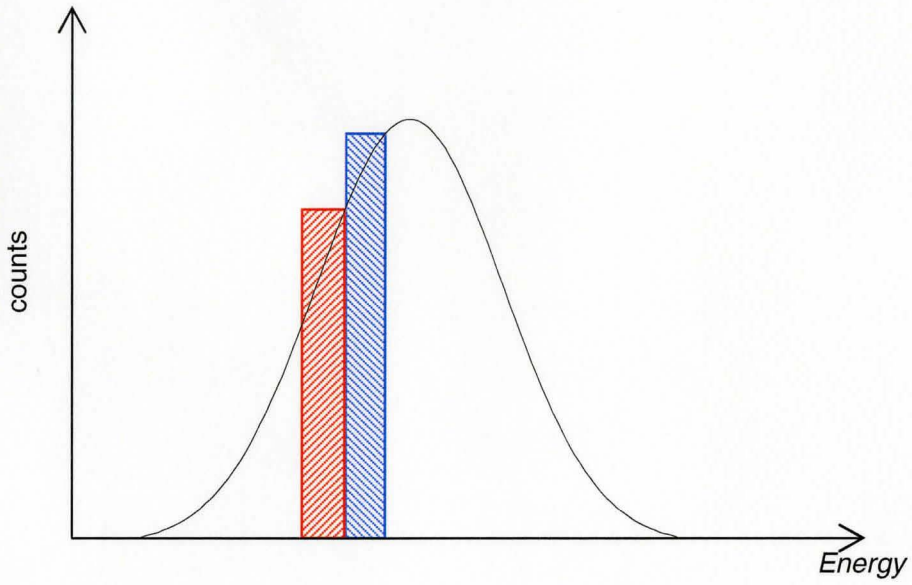

Figure 3.18: Energy Spectrum for a fixed scattering angle.

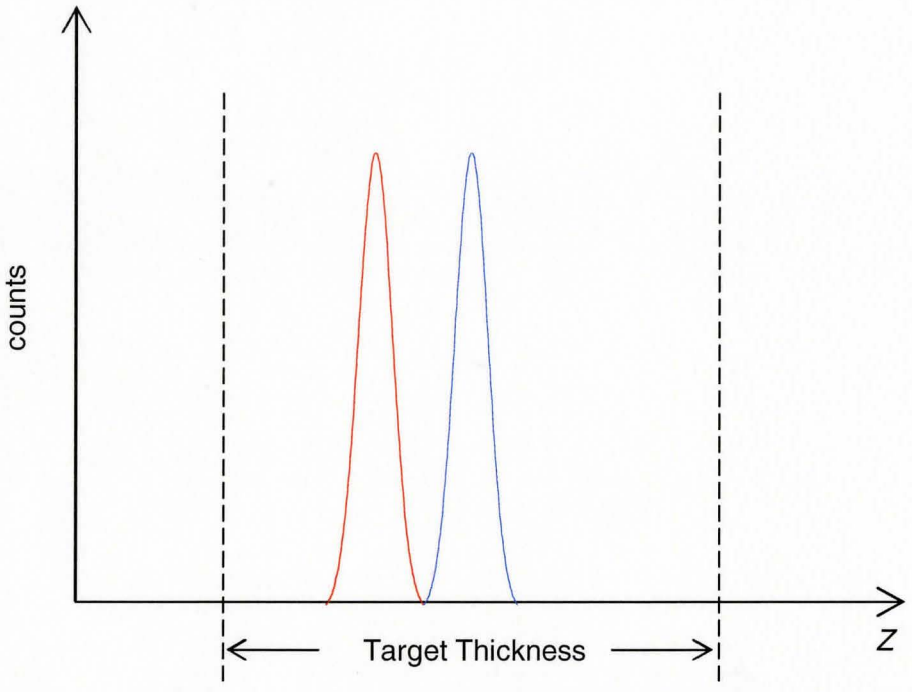

Figure 3.19: Locations corresponding to the energy cuts in above figure. Red peak corresponds to red cut above and blue peak to blue cut.

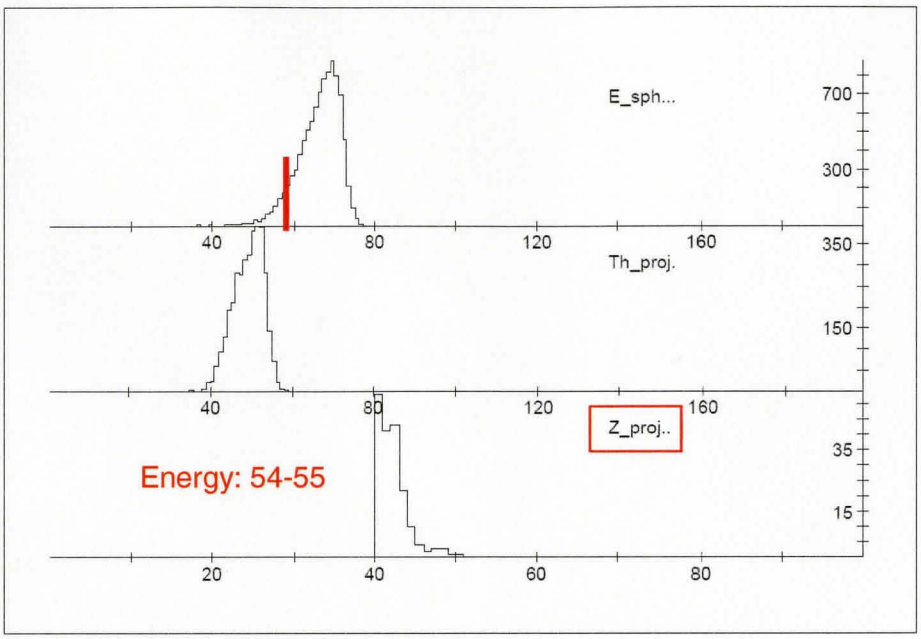

Figure 3.20: Energy cut: channel 54-55, angle cut: channel 40-42

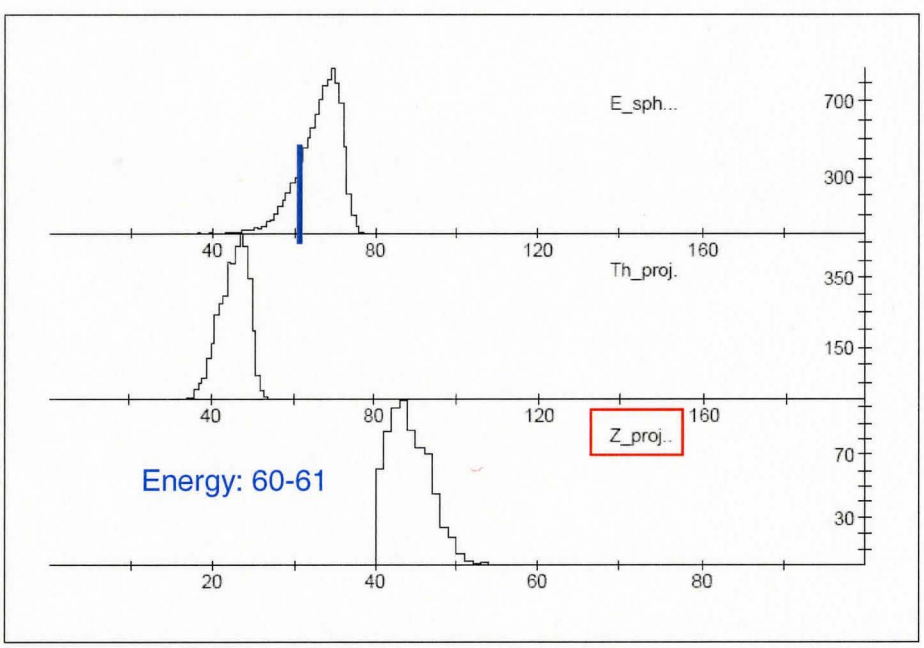

Figure 3.21: Energy cut: channel 60-61, angle cut: channel 40-42

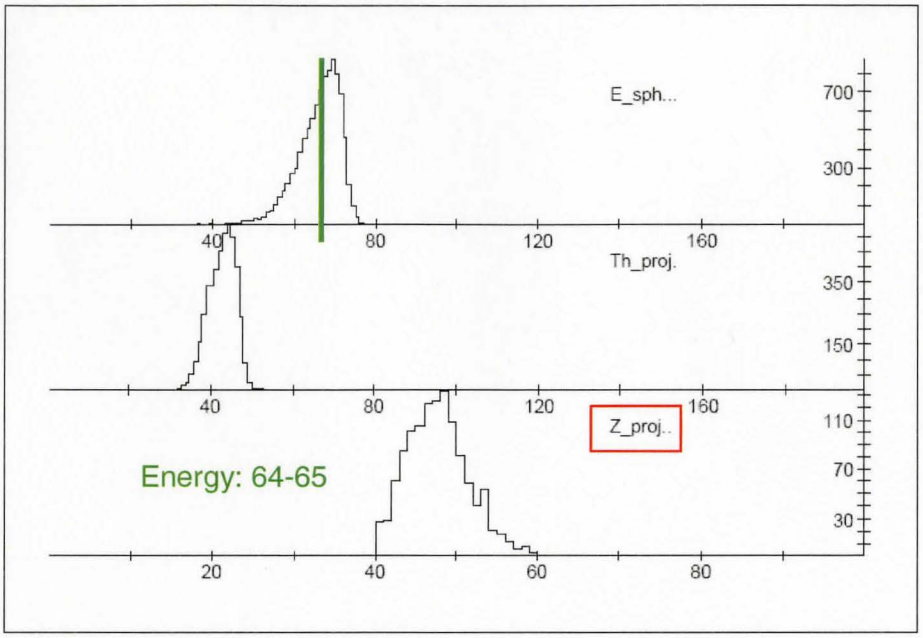

Figure 3.22: Energy cut: channel 64-65, angle cut: channel 40-42

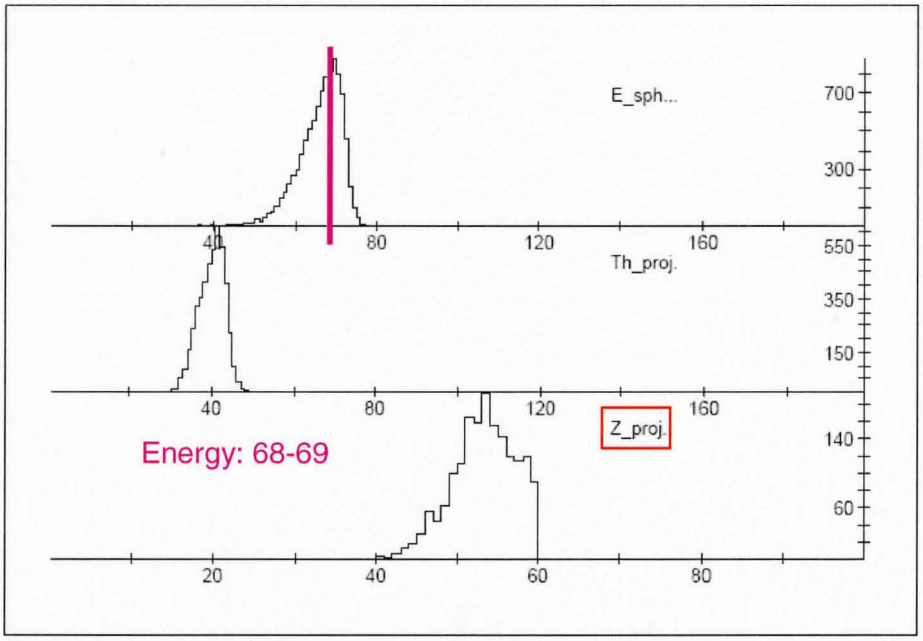

Figure 3.23: Energy cut: channel 68-69, angle cut: channel 40-42

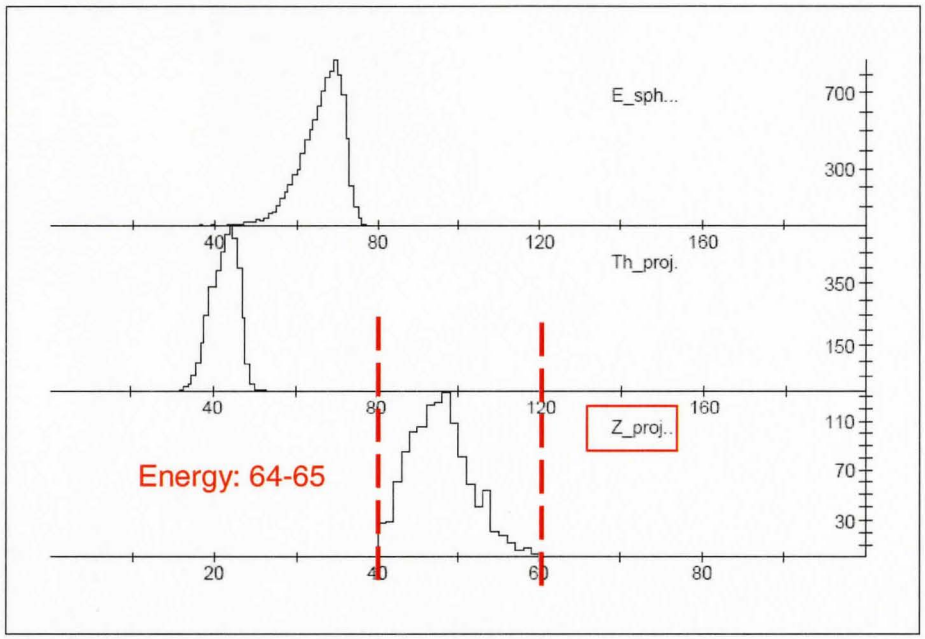

Figure 3.24: Main result of the simulations: The location distribution for a cut covers the whole thickness of the target. (angle cut: channel 40-42)

Chapter 4

Experimental Tests

In order to obtain the optimal working conditions for the CD detector and also to avoid damaging the expensive and fragile CD detector, we first used a test detector—a silicon ULTRA detector— to test all the electronics. Only after finishing that did we begin to instrument the CD detector and perform energy measurement tests with it.

4.1 Test Station

The test station for the CD detector was assembled in our laboratory at McMaster University. All the tests for the CD are being performed here and after that the working detector system will be moved to TRIUMF at Vancouver and integrated with the future TIGRESS facility in the ISAC-2 experiment hall. The test station primarily consists of a vacuum system and an electronics and data acquisition system. Figure 4.1 shows the full test station.

4.1.1 Vacuum System

The main part of the vacuum system is a stainless steel vacuum chamber, inside of which the CD detector and the test source were mounted, as shown in figure 4.2.

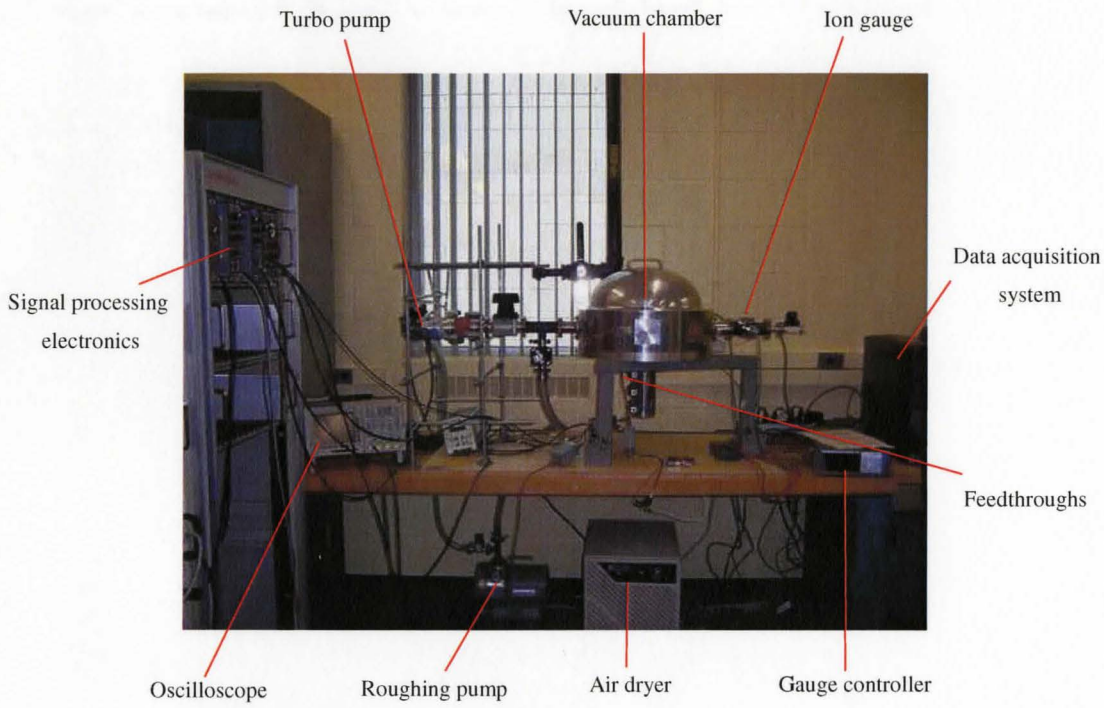

Figure 4.1: The test station for the CD detector

All feed-throughs, such as for the bias and signals, of the detector and electronics are located on the bottom plate of the chamber.

The required vacuum condition inside the chamber is achieved by a roughing pump (VARIAN SH-100 Dry Scroll Vacuum Pump) and together with a turbo pump (VARIAN Turbo-V70). The chamber pressure is measured by an ion-gauge (VARIAN 564 Ionization Gauge Tube) and read out by a gauge controller (VARIAN senTorr Gauge Controller). These parts are shown in figure 4.3. When operating, we first turn on the rough pump till the gauge controller reads 10^{-3} Torr and then turn on the turbo pump. The best vacuum condition we can achieve with our pumping system is of the order of 10^{-5} Torr. It is well known that applying a bias to a double-sided silicon detector in the 10^{-1} Torr gas pressure range can be damaging to the detector; therefore pumping and venting should never be done with the detector bias on.

The turbo pump is located at the end of the turbo pump line and supported

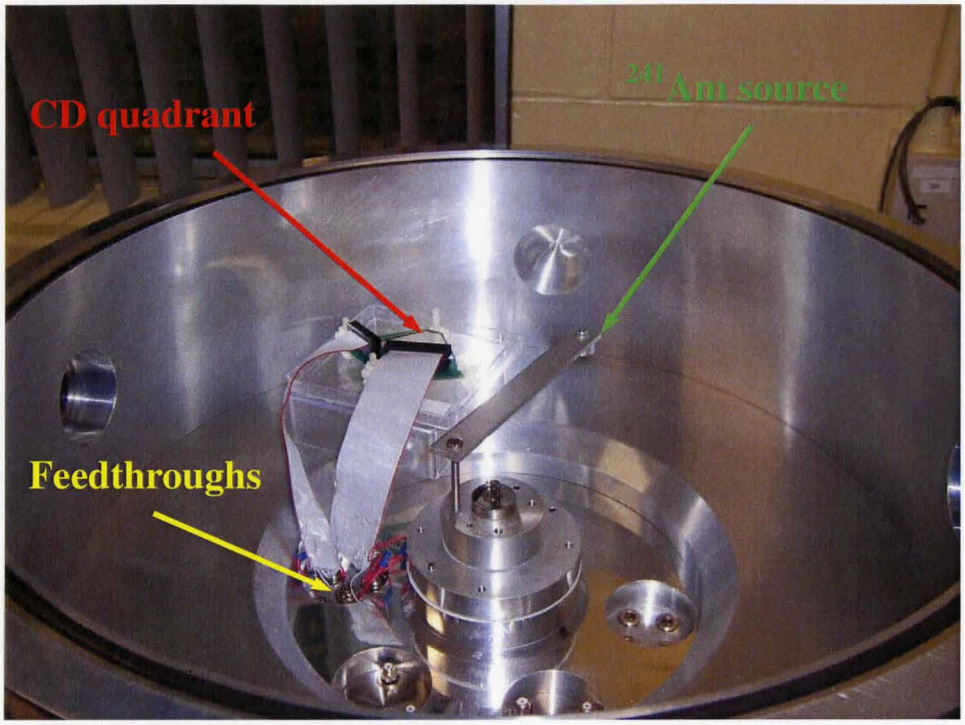

Figure 4.2: Vacuum chamber.

only by a spring system hung on a support frame designed to damp mechanical vibrations. In addition, a vibration damper was used in the coupling between the turbo pump and the chamber. However, we have found that vibrations from the turbo pump still introduced unwanted noise into the detector signal. On the other hand, we also found that only keeping the rough pump on was enough for our tests.

4.1.2 Electronics and Data Acquisition System

The CD detector has 16 front strips and 24 back strips per quadrant, which results in a total of 160 detector elements for the entire detector. Therefore, to instrument all the elements, the same number of charge-sensitive preamplifiers is needed. For our test, we only used 8 channels of preamplifiers placed in a shielded box (SWAN RESEARCH BOX8CHLEMO). So, of the 160 detector elements of the CD, we

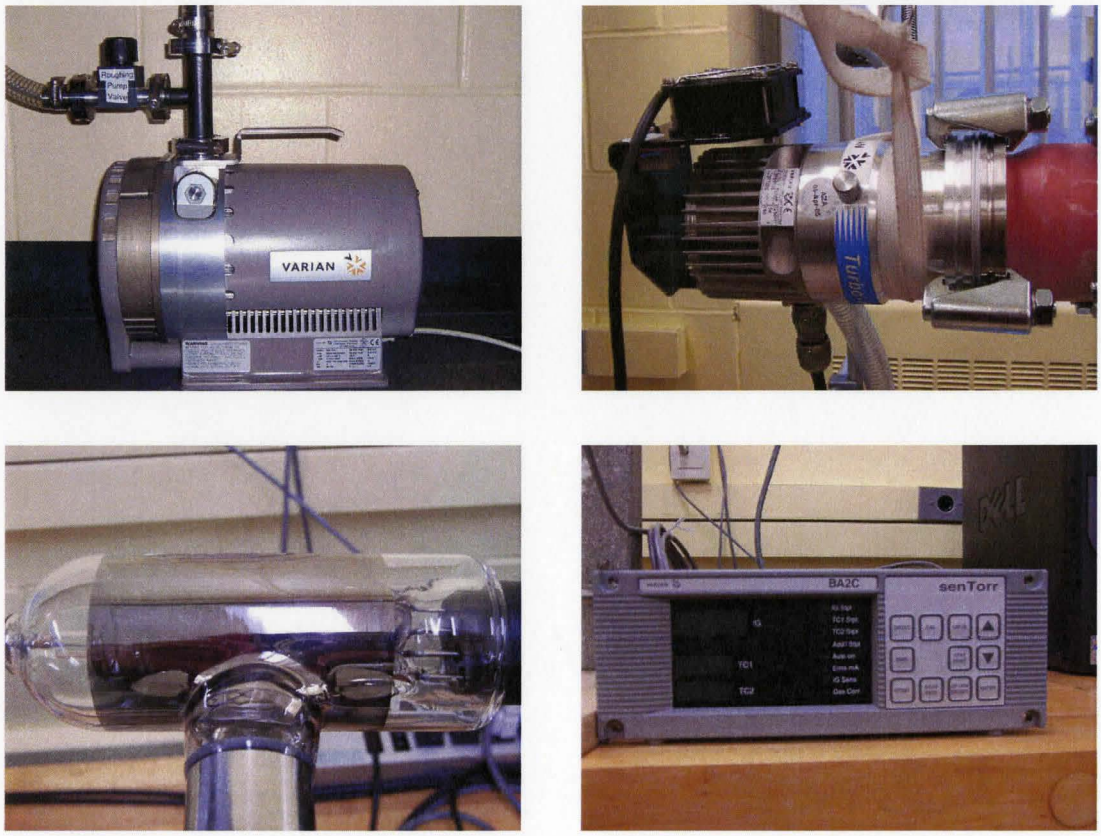

Figure 4.3: Photographes of other parts of the vacuum system.

Top left: rough pump Top right: turbo pump
Bottom left: ion gauge Bottom right: gauge controller

only instrumented 8 elements for initial tests. All tests for the CD were performed with the SWAN preamplifier. There are also two other preamplifiers, Canberra 2004DM and Ortec 142, which were only used in the ULTRA detector tests for looking for the optimal working condition of the detector system. Each preamplifier has inputs for the detector signal, preamplifier power, detector bias, and a test pulse. The output of the preamplifier is fed into an ORTEC 572A amplifier and then the amplifier output is input directly into the acquisition system, an Ortec TRUMP PCI card directly plugged inside the PC case. The associated software for data acquisition is the Ortec MAESTRO package, which is also used to display and analyze data. A digital oscilloscope is also used for displaying signals. The

amplifier together with the ORTEC 4001C BIN power supplies for the preamplifiers and the amplifier are housed in a CANBERRA NIM BIN. We also have an ORTEC 710 QUAD Bias Supply in place for providing detector bias for the CD detector tests. We did not use it for ULTRA detector tests, where instead we used batteries. Figure 4.4 and figure 4.5 show photographs of the electronics and data acquisition system (DAQ).

Figure 4.4: Photographs of electronics.

Top left: SWAN preamplifier Top right: Canberra preamplifier
Bottom left: ORTEC preamplifier Bottom right: ORTEC amplifier and bias supply

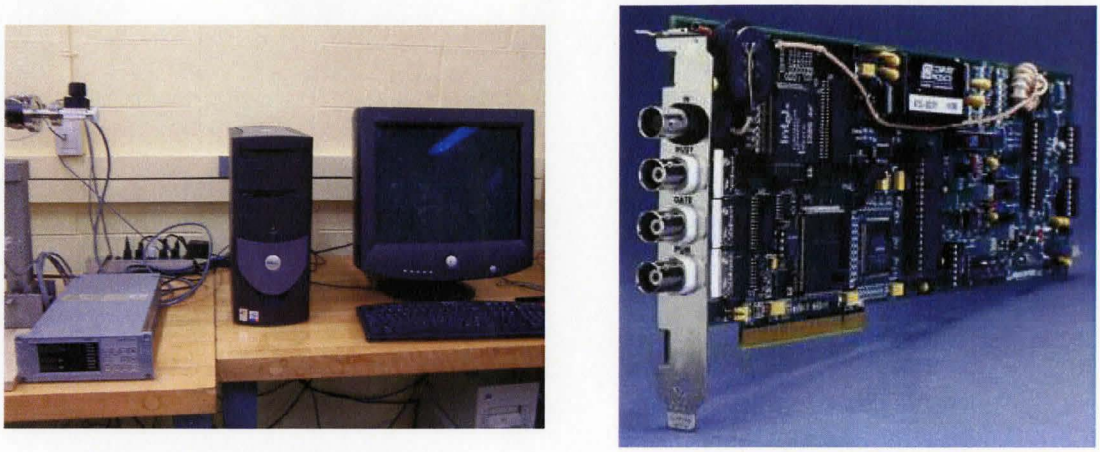

(a) (b)

Figure 4.5: Photographs of the data acquisition system. (a) PC; (b) Ortec TRUMP PCI card in the PC case.

4.2 Tests with ULTRA Detector

The ULTRA detector used in our tests is an ion-implanted-silicon surface barrier detector for alpha and beta spectroscopy manufactured by the ORTEC company [35]. The guaranteed energy resolution of the ULTRA detector by the manufacturer is 20 keV and the maximal detector bias voltage is 100 V. Figure 4.6 is a photograph of our ULTRA detector and its setup in the vacuum chamber.

4.2.1 Testing the Electronics

We have tested three different preamplifiers: ORTEC preamplifier, Canberra preamplifier and SWAN research preamplifier. Among them, the SWAN preamplifier was the one thereafter used for the CD tests and the other two were just used here to check the noise condition of the detector system.

The alpha source we used in these tests is ^{241}Am of about 0.1 microcurie, which primarily emits alpha particles with energy of 5.486 MeV (85.2%), 5.413 MeV(12.8%) and 5.389 MeV(1.3%). What we are concerned about for our energy resolution tests are those with energy of 5.486MeV. The energy resolution of the

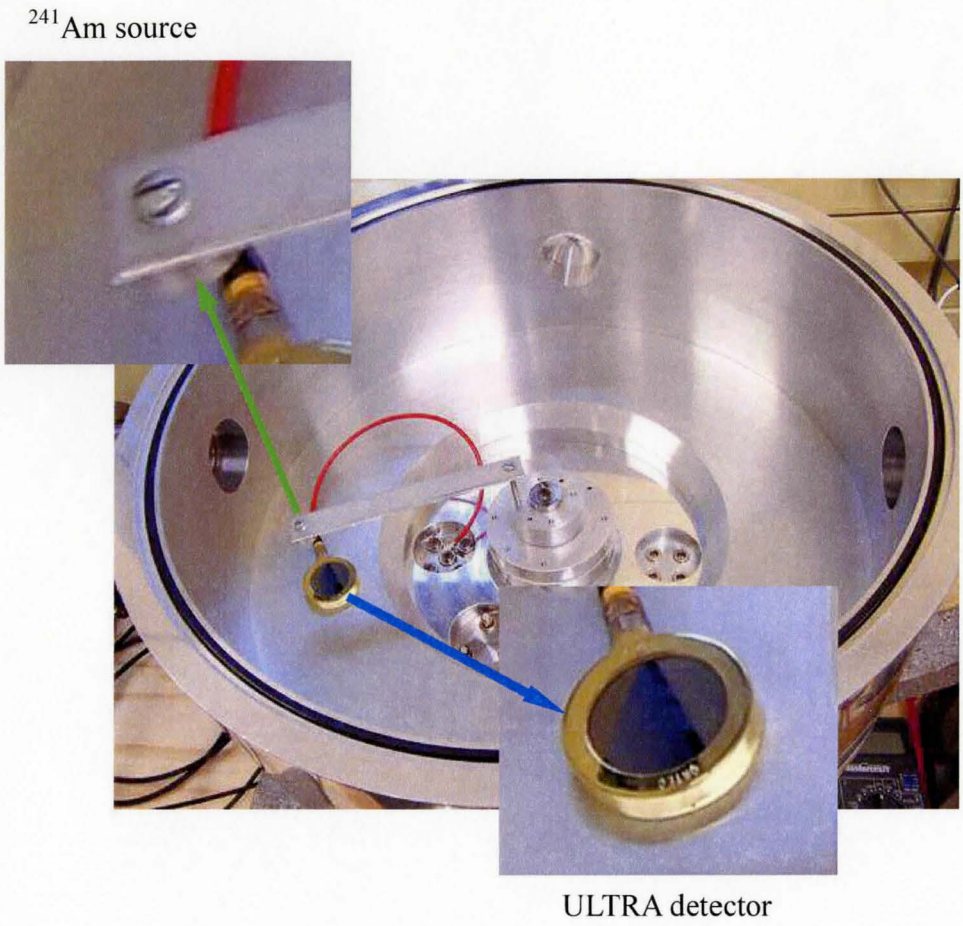

Figure 4.6: ULTRA detector setup.

ULTRA detector around this energy was measured under different conditions, such as different preamplifiers, different shaping time of the amplifier, different detector bias and different source-to-detector distance. We also used a test pulser for comparison. The test results under different working conditions are given in the following figures. Figure 4.7 shows measured alpha spectra using different preamplifiers. Figure 4.8 shows measured alpha spectra for different shaping times. Figure 4.9 shows measured alpha spectra for different detector biases. The energy resolution for these conditions are listed in table 4.1. Compared with the simulation results in Chapter 3, these measured energy resolution are worse, which is caused mainly by the effect of the electronics noise and the thickness of the alpha source in real

experiments.

From these tests, it is shown that the best spectrum was obtained with the Canberra preamplifier under a working condition of 2 μs shaping time and the highest bias, with an energy resolution much better than the guaranteed 20 keV. But in fact, the Swan preamplifiers were finally used for the later CD tests and the Ortec and the Canberra ones were only used here for testing the electronic setup.

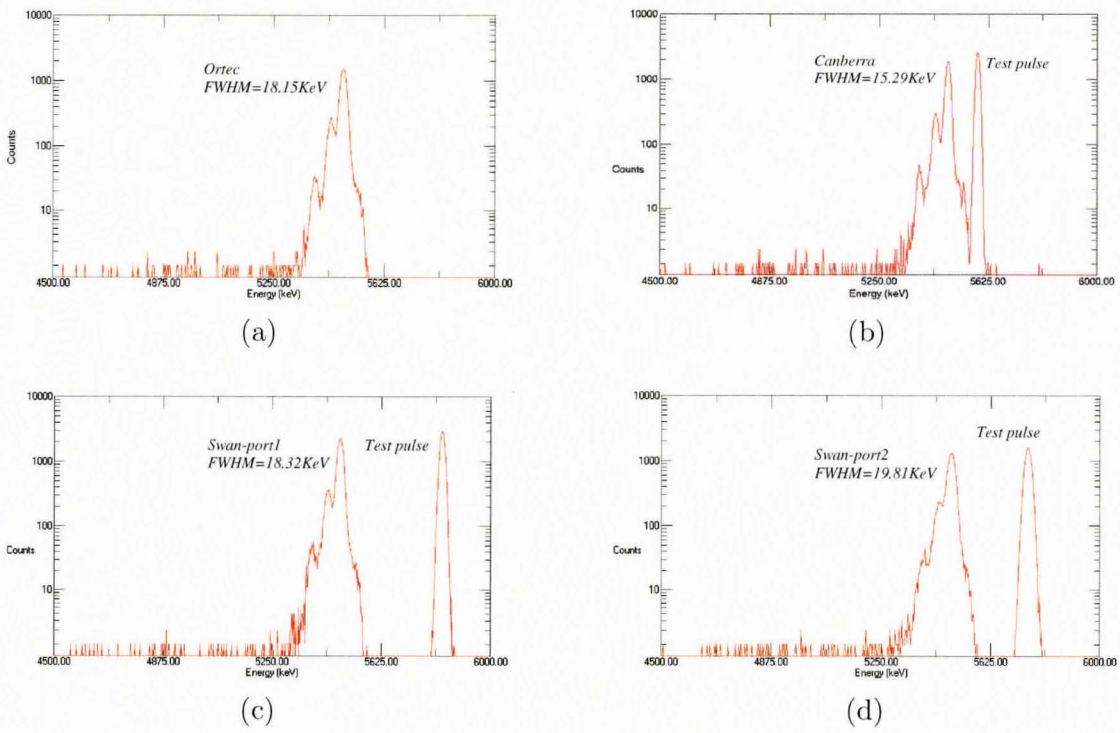

Figure 4.7: Alpha spectrum with different preamplifiers. (a) ORTEC preamplifier; (b) Canberra preamplifier; (c) SWAN preamplifier port1 (d) SWAN preamplifier port2. The port1 and port2 preamplifiers have the same time constant but different capacitances: 2pf and 6pf respectively, which will be used for different experiments with TIGRESS: one for (d, p) experiments and the other one for Coulex experiments .

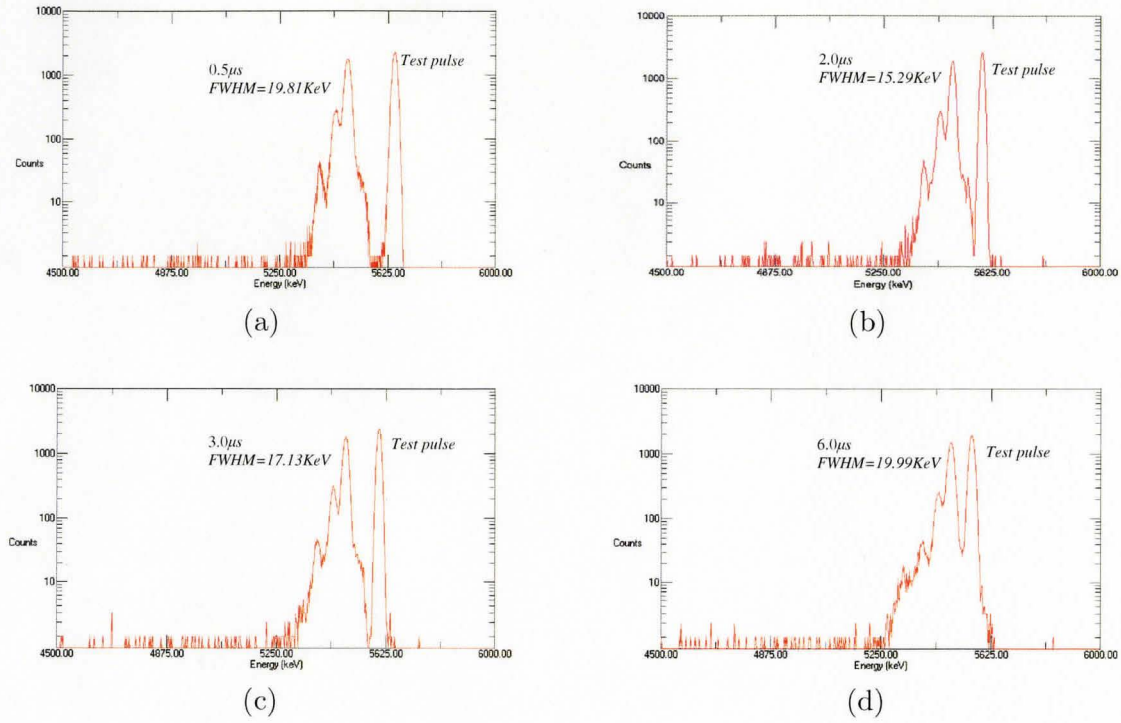

Figure 4.8: Alpha spectrum with different shaping time. (a) 0.5 μs; (b) 2 μs; (c) 3 μs; (d) 6 μs.

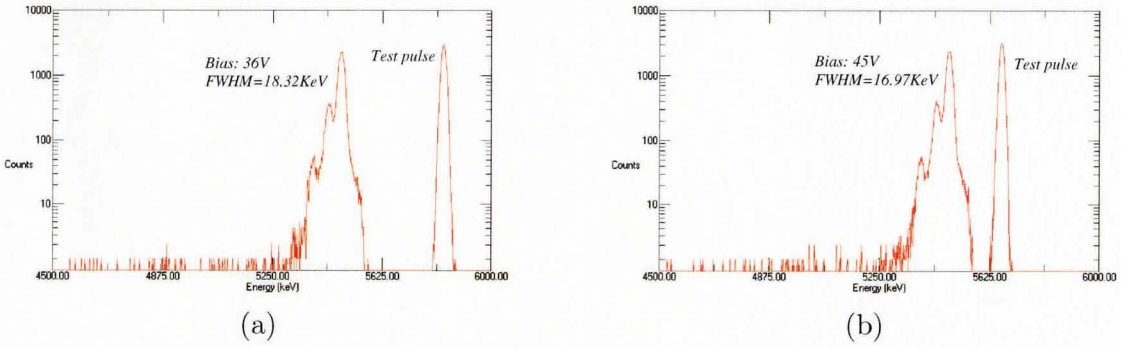

Figure 4.9: Alpha spectrum with different detector bias. (a) 36 V; (b) 45 V.

Preamplifier	***FWHM (keV)***
ORTEC	18.75
Canberra	15.29
SWAN Port-1	18.32
SWAN Port-2	19.81
Shaping time of the amplifier (μs)	
0.5	19.81
2.0	15.29
3.0	17.13
6.0	19.99
Detector bias (V)	
36	18.32
45	16.97

Table 4.1: ULTRA detector measured energy resolution for different preamplifiers, shaping time and detector bias.
(When using different preamplifiers, the shaping time was kept at 2.0 μs and the bias at 36 V. Measurements for different shaping times were made with Canberra preamplifiers and with a bias of 36 V on. Measurements under different detector biases were made for SWAN preamplifiers at port-1 with the shaping time set at 2.0 μs. The runtime for all measurements was set to 600 s.)

4.3 CD Detector Testing

The CD detector tested in our lab will act as an auxiliary detector detecting the scattered heavy ion beam particles or the target recoils in coincidence with γ-ray detection in the TIGRESS spectrometer. The aim of the testing is to carry out energy resolution measurements for each strip of the CD detector and make an energy calibration. In addition, 8 channels out of the 40 channels per quadrant are expected to be instrumented as we only have 8 SWAN preamplifiers.

4.3.1 CD Detector in our lab

The geometry and properties of the CD detector have been described in chapter 2. The actual CD detector in our lab is shown in figure 4.10, which was fabricated by MICRON Semiconductor Ltd. [36]. Figure 4.11 shows the front and the back views of one of the four quadrants. Each quadrant has two high-density 0.025" IDC connectors at the periphery of the PCB board,bringing out a total of 40 signals to the ribbon cables—16 signals from the front strips and 24 signals from the back strips. The tiny bronze wires connecting the strips to the connectors are very fragile and careful attention must be paid when conducting any operations on the CD.

4.3.2 The Setup for the Tests

To avoid damaging the whole CD detector, only one quadrant of the CD detector was chosen for testing. The setup for the tests is shown in figure 4.12. The CD quadrant lies in the vacuum chamber and the ^{241}Am source is right above the pixels to be tested at a distance of 3-4 cm. The sector strips on the rear ohmic side are grounded to a common ground and the annular strips on the front junction side are biased to -100 V, which is the full depletion voltage indicated by the manufacturer.

Figure 4.10: The CD detector in our lab & a real CD disk.

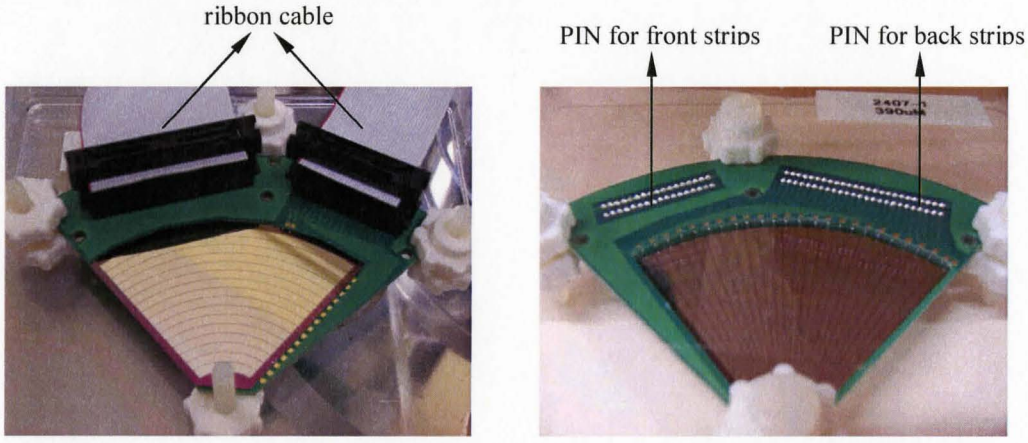

Figure 4.11: Front and back view of the CD detector.

4.3.3 Energy Resolution Measurements

To bring out all 40 signals from the strips on both sides of the CD at one time, 40 preamplifiers are needed. The SWAN preamplifier module used in testing only provides 8 channels. In our initial testing, four channels were instrumented to obtain the signals from 4 detector elements out of 40, which results in four detector pixels , two signals for each — one from the front ring and one from the back sector.

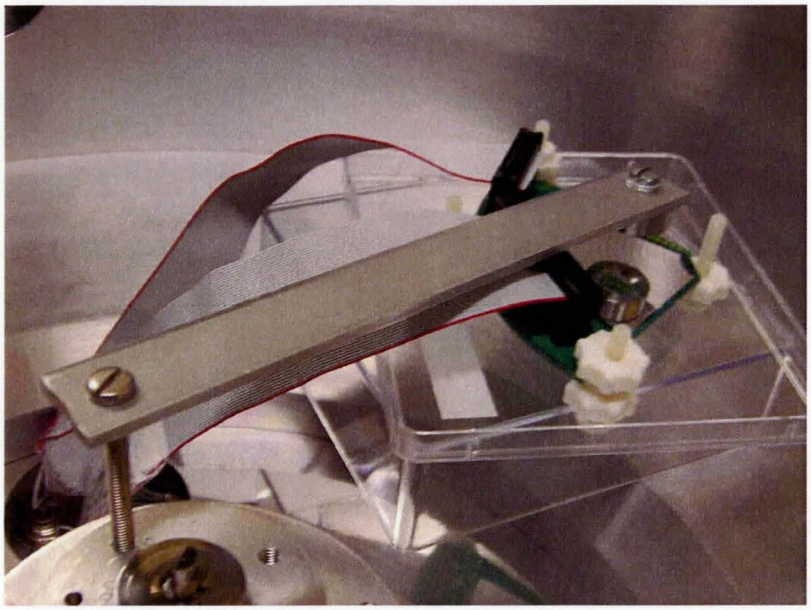

Figure 4.12: Photograph of testing setup for the CD detector.

It was found that whether or not the preamplifiers for other strips were installed made the signals from the tested strips different, an effect which was verified by a computer simulation of the circuit[1]. To eliminate or reduce this effect caused by the absence of the preamplifiers for other strips, a capacitor was connected to each of them to make an analog of a preamplifier. But later it was found that those capacitors can not work quite like the preamplifiers and the difference mentioned above still existed.

We also noticed that from each ring or sector, besides the primary pulses, secondary pulses were observed with the polarity opposite to the primary ones and amplitude smaller than that of the primary ones. It was believed that the smaller pulses resulted from a coupling effect between the signals from the ring and the sector at each pixel since the silicon CD detector has capacitance in the depletion region between the front strips and the back strips. This was also verified by a computer simulation using a capacitor to model each detector pixel with the corresponding capacitance of each pixel. But this effect will not be a problem,

[1]The circuit simulations were made using a simulation program named CircuitMaker2000.

since it is thought to be a normal inter-strip event and can easily be eliminated by requiring equal energy from the front junction side and the back ohmic side of the CD detector. To do this, a coincidence gate signal generated from the outputs of the ring and sector strips at a pixel was introduced to the data acquisition system (DAQ) through an Ortec universal coincidence unit 418A, so that signals were collected by the DAQ only when the coincidence happened. Figure 4.13 shows the alpha spectra acquired from both sides at a pixel of the CD quadrant with the alpha source not collimated. The energy resolution of the front strip is FWHM = 22.85 keV, below the guaranteed resolution 30 keV, whereas that of the back one is FWHM = 40.33 keV. These energy resolution are worse than those in ULTRA testing. The reason is that, besides the same effect of the electronics noise and the thickness of the alpha source as in ULTRA testing, CD detector's back sectors potentially have an intrinsic contribution to the overall energy resolution.

The spectra indicate that the front annular strip has better energy resolution than the back sector strip. This result was also found in the results from other pixels under the same condition and was orientation-independent with respect to the direction of the alpha source emission. As it is known from above that the preamplifiers play an important role in the measurements, it is thought that introducing all preamplifiers to all detector elements will improve the performance and make the results better. Due to the limited number of the preamplifiers in our laboratory, further tests will be made to utilize all of our current 8 preamplifiers, by grouping 4 front detector elements to the same preamplifier and grouping 6 detector elements on the back side; that means only 8 preamplifiers are required, 4 for the 16 front annular strips and 4 for the 24 back sector strips.

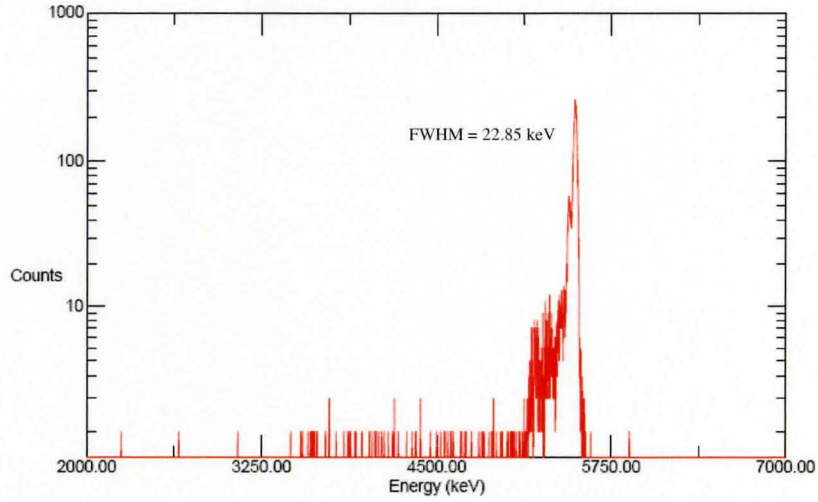

(a)

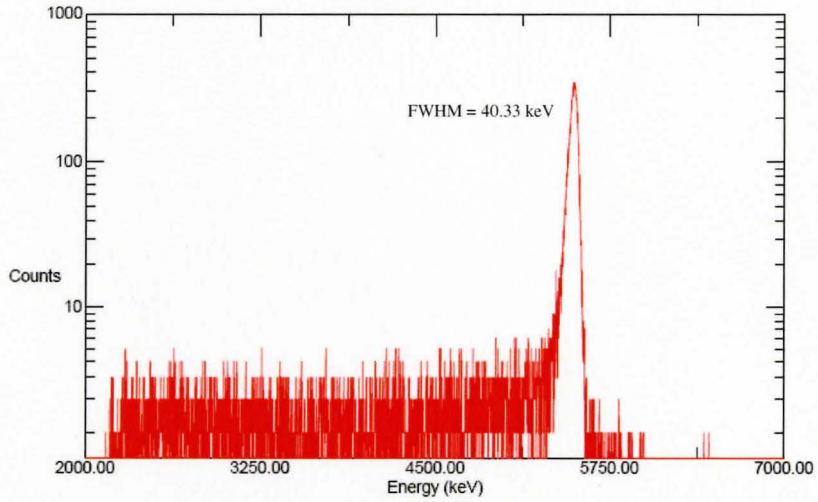

(b)

Figure 4.13: Alpha spectra acquired from both sides at a pixel of a CD quadrant: (a) the spectrum from the front annular strip, run-time about 3600s; (b) the spectrum from the back sector strip, run-time about 9000s.

Chapter 5

Conclusions and future work on the CD Detector in our lab

With GEANT4 simulations, the CD detector has been modeled and tested using a virtual ^{241}Am alpha source. The results have shown that the simulations work very well. Further locating simulations using an alternate Al-sphere detector were performed by shooting 330 MeV ^{110}Sn onto a 2 μm ^{58}Ni target. This simulation also works; that is, by placing different energy cuts on the energy spectrum of the scattered ions obtained by the Al-sphere at a specific angle, we can actually get different position distributions corresponding to the cuts, with the peaks of the distributions moving along the depth of the target thickness. Although these results indicate the possibility of locating the scattering position in the target by this simulation, which can provide useful information for Doppler correction of γ-ray detection in TIGRESS, it is not very useful and efficient since the position distributions cover the whole range of the thickness of the target. When there are only a few scattering events, the scattering positions can not be definitely determined, or they can be determined probabilistically at best. This problem has also been seen in other simulations using different thicknesses of the target. It might be caused by the different energy losses of the scattered ions during the interactions with the target ions. Because the angle cut set in the simulations

was not a definite value but a small range of angles, which allowed the scattered beam ions not to have the completely same scattering angle and also resulted in an energy distribution over this small range, some of these ions might transfer different energies from the majority to the target ions during the collision; but combined with the different energy loss caused by ionization, these ions may have the same energy upon leaving the target as the others that were scattered from different spots along the depth of the target thickness, but scattered into the same angle range, about 0.5 degree wide. We might be able to improve the above situation by decreasing the width of the angle cut in the simulations; however, this is not useful since in reality the resolution of the scattering angle is limited by the finite solid angle of real CD pixel. Nevertheless, our simulations can be used to provide probability distributions of scattering locations, which can be useful for Doppler correction of γ-rays detected with TIGRESS.

Experimental tests have been performed first with a standard silicon ULTRA barrier detector to test all the electronics and experimental conditions for the CD tests. A SWAN preamplifier module, which can house 8 preamplifier units inside, has been used to bring out 8 signals from the 8 strips, which can give information for at most a total of 4×4 individual pixels. There exists a coupling effect between the p junction side and the n ohmic side, which creates a smaller polarity-inverted pulse relative to the regular pulse for each strip. This effect can be easily eliminated by requiring equal energy from the front strip and the back strip at a pixel. The energy resolution guaranteed by the manufacturer is about 30 keV for a 5.486 MeV alpha source. The testing results are satisfactorily below this level. Subsequent tests for a quadrant of our CD detector has given nice alpha spectra for the front annular strip but spectra with worse resolution for the back sector strip. It is thought that instrumenting all 40 channels with preamplifiers will make improvements. What can be presently done with the limited number of the preamplifiers in our laboratory is to group a few detector elements into one channel. That will make it possible for the whole quadrant work only with 8

preamplifiers. This next phase of tests is already in progress.

In the near future, measurements of the energy resolution for all strips will be completed and all four CD quadrants will be tested. We also expect to be able to have all of the 40 channels instrumented at the same time for the full quadrant testing.

Appendix A

Fundamentals about using GEANT4

Here the fundamentals of some key components of GEANT4 are described. All the examples are directly quoted from the GEANT4 manual [37].

A.1 Geometry

To define a detector system in a simulation, we need the representation of the geometrical elements, their shapes, their materials and electronic structure of the system, together with visualization attributes and user defined properties. In GEANT4, these things can be done when defining the geometry of the detector system. The geometry in GEANT4 is, in fact, made of a number of volumes. Each volume represents an object with its shape and its physical characteristics, except the largest volume called "World" volume, which in fact is a virtual volume and contains, with some margin, all other volumes in the detector geometry. A small volume can be placed in a big volume. We call the big one "mother" volume and the small one "daughter" volume. A coordinate system of the mother volume is used to specify where the daughter volume is placed.

To create a volume, firstly, one should draw the shape of the volume, which can be done by creating a solid in GEANT4. A solid is a geometrical object that has a shape and specific values for each of that shape's dimensions. GEANT4 has a library of predefined solids (box, torus, cones, cylinders, etc.), and we can thus

choose any one we need and just define its name and its extent along each of the Cartesian axes. For examples, to create a box, we can just add the following C++[1] code in the source file of the *detector construction* part:

```
G4double expHall_x = 3.0*m;
G4double expHall_y = 1.0*m;
G4double expHall_z = 1.0*m;
G4Box* experimentalHall_box
        =new G4Box("expHall_box", expHall_x expHall_y, expHall_z);
```

This creates a box named "expHall_box" with extent from -3.0 meters to +3.0 meters in X axis, from -1.0 to 1.0 meters in Y, and from -1.0 to +1.0 meters in Z.

After creating the solid shape for the volume, the concept of "logical volume" is used to add other attributes of the volume, like materials of the volume, to the solid. Just below the code above, one can create a simple logical volume filled with argon gas for the box by entering the code:

```
G4LogicalVolume* experimentalHall_log;
        = new G4LogicalVolume(experimentalHall_box, Ar, "expHall_log");
```

This creates a logical volume named "expHall_log" for the box created above and this logical volume contains the attributes of the box.

Till now, there is only one more thing that is required to complete the geometry construction of the volume, that is, to place the volume inside of an already existing one. There is an exception that the "world" volume, usually created as the experiment hall, does not need to be placed in any other volume. To finish the placement, one needs to decide where to place its center and how to rotate it. This work can be done by creating a physical volume. For example, to place a tracker used to track the particles passing through it, which has been created and has its logical volume named "tracker_log". Inside the volume of the experimental hall above, one can just enter the following code:

```
G4double trackerPos_x = -1.0*m;
G4double trackerPos_y = -1.0*m;
```

[1]For C++ programming, refer to [38, 39]

```
G4double expHall_z = 1.0*m;
G4VPhysicalVolume* tracker_phys
= new G4PVPlacement (0,
                     G4ThreeVector (trackerPos_x, trackerPos_y,trackerPos_z),
                     "tracker",
                     Tracker_log,
                     experimentalHall_log,
                     false,0)
```

This places the logical volume with name "tracker_log" at the origin of the mother volume "experimentalHall_log", shifted by one meter along X and unrotated. The resulting physical volume is named "tracker".

Now the construction of the geometry for a volume is finished and other volumes can be created in the same way.

A.2 Materials

When defining the geometry, one needs to provide information on the materials to the detector system, such as the materials of the detector, the target, the chamber, etc. The class of the materials must contain the information on the properties of the atoms and matter in these materials. In nature, general materials (chemical compounds, mixtures) are made of elements and elements are made of isotopes. In GEANT4, there is a library of preconstructed elements, isotopes and materials, and users can also create new materials through three classes: ***G4Isotope***, ***G4Element***, and ***G4Materials***.

The ***G4Isotope*** class describes the properties of isotopes:

- Atomic number
- Number of nucleons
- Atomic mass
- Shell energy
- Quantities such as cross section per atom, etc.

An example of an isotope definition is shown by the following code:

```
G4Isotope* U5 =
        new G4Isotope(name="U235", iz=92, n=235, a=235.01*g/mole);
```

This creates an isotope named ^{235}U with atomic number 92, 235 nucleons and atomic (molar) mass 235.01 g/mole.

The G4Element class describes the properties of elements:

- Effective atomic number
- Effective number of nucleons
- Effective mass per mole
- Number of isotopes
- Shell energy
- Quantities like cross section per atom, etc.

An example of an element definition is shown by the following code:

```
G4Element* elH =
        new G4Element(name="Hydrogen", symbol="H", z=1, a=1.01*g/mole);
```

This creates an element named Hydrogen with symbol "H", atomic number 1 and atomic (molar) mass a=1.01 g/mole .

Also, an element can be created from isotopes by their relative abundances when the elements consist of different percentage of isotopes. An example of an element definition from isotopes is shown by the following code:

```
G4Element* elU =
  new G4Element(name="enriched Uranium", symbol="U", ncomponents=2);
elU->AddIsotope(U5, abundance= 90.*percent);
elU->AddIsotope(U8, abundance=20.*percent);
```

This creates an element with the name "enriched Uranium", symbol "U" and two components: 90% isotope U5 (Uranium-235) and 10% isotope U8 (Uranium-238).

The ***G4Materials*** class describes the macroscopic properties of matter:

- Density
- State
- Temperature
- Pressure
- Macroscopic quantities like radiation length, mean free path, stopping power dE/dx, etc

An example of an simple material definition is shown by the following code:

```
density =2.33*g/cm3;
a =28.09*g/mole;
G4Material* Si = new G4Material(name="Silicon", z=14, a, density;
```

This creates a simple material — Silicon.

There are also two other ways to define a material: by defining a chemical molecule from elements by components, and by defining a mixture from elements by fractional mass. For example, to define the gas molecule CO_2, one just needs to add the following code in the program for detector construction:

```
density = 27.*g/cm3;
pressure = 50.*atmosphere;
temperature = 325.*kelvin;
= new G4Material ("CO2", density, nComponents=2,
        kStateGas, temperature, pressure);
CO2->AddElement(elC, nAtoms=1);
CO2->AddElement(elO, nAtoms=2);
```

This creates the CO_2 molecule through its density, chemical composition, state, temperature and pressure.

A.3 Particles

There are a large number of elementary particles and nuclei in the world. In GEANT4, there is a library of predefined particles covering all the particles we know and the user can just select the relevant particles from the library and add them to the program in the *physics list* part. There are three classes of definitions for a particle in GEANT4, each of which characterizes a different aspect of the particle's properties. The ***G4ParticlesDefinition*** class includes the static information of the particle, such as name, mass, spin, life time, and decay mode. The ***G4DynamicParticle*** class provides the dynamic information of the particle, such as energy, momentum, polarization, and proper time. The ***G4Track*** class has all the information necessary for tracking a particle in a detector simulation, such as time, position, and step length.

The user can also define any particles they want. The categories of particles in the library are:

- leptons
- mesons
- baryons
- bosons
- short-lived particles
- ions

A.4 Physics processes

When an incident particle with some specific energy impinges on a target of some thickness in a GEANT4 simulation, what will happen? The program has to know, according to the properties of the incident particles and the target particles, their relative position, and the external conditions, how they interact, etc. That is the role of the physics process in the program. In a simulation, users can just select the

relevant processes from the seven major categories and add them to the program in the *physics list* part:

- electromagnetic
- hadronic
- transportation
- decay
- optical
- photolepton-hadron
- parameterization

A.5 Condition Setup

This is the final step to complete a simulation. As the detector geometry has been constructed and the physics processes have been added for a simulation, what is left is to implement the simulation and to gain control of the simulation at various states, e.g., controls of the Run, Event, Track and Step. GEANT4 provides five optional virtual methods to enable users to customize the simulation to their specific situations. They are:

- ***G4UserRunAction***

  This is for actions at the beginning and end of every run. It can be used, for a particular run, to set variables which affect the physics table (such as production thresholds), to initialize and book histograms at the beginning and analyze the results from the processed run at the end.

- ***G4UserEventAction***

  This is for actions at the beginning and end of every event. It can be used, for a particular event, to initialize and book histograms at the beginning and analyze the results from the processed event at the end.

- ***G4UserStackingAction***

  This is a class for controlling the various track stacking mechanisms and customizing access to the track stacks.

- ***G4UserTrackingAction***

  This is for actions at the creation and completion of every track. It can be used, for a particular track, to create a predefined trajectory and decide whether the trajectory should be stored or not at the beginning and analyze the results from the processed track at the end.

- ***G4UserSteppingAction***

  This is a class representing actions taken place by the user at each end of stepping. It is used for customizing the behavior at every step.

Apart from these user-defined actions, users can also define their own visualizations for the whole detector system. In Chapter 3, a simple example is given to show how to use GEANT4.

Bibliography

[1] C. E. Svensson, P. Amaudruz, *et al.*, "TIGRESS: TRIUMF-ISAC gamma-ray escape-suppressed spectrometer," *J. Phys. G: Nucl. Part. Phys.*, vol. 31, pp. S1663–S1668, 2005.

[2] R. Laxdal and R. Baartman, "Design Optimization Of the Proposed ISAC-2 Project at TRIUMF," in *Proceedings of the 1999 Particle Accelerator Conference*, (New York), 1999.

[3] J. D'Auria, L. Buchmann, D. Hutcheon, P. Lipnik, D. Hunter, J. Rogers, R. Helmer, U. Giesen, A. Olin, and P. Bricault, "A Facility for Studying Radiative Capture Reactions Induced with Radioactive Beams at ISAC ," *Nuclear Physics A*, vol. 621, p. 599c, 1997.

[4] C. E. Rolfs and W. S. Rodney, *Cauldrons in the Cosmos.* The University of Chicago Press, 1988.

[5] A. Friedman, "On the Curvature of Space," *Z.Phys.*, vol. 10, p. 377, 1922.

[6] G. Lemaître, "A homogeneous Universe of constant mass and growing radius accounting for the radial velocity of extragalactic nebulae," *Annals of the Scientific Society of Brussels*, vol. A47, p. 49, 1927.

[7] G. Gamow, "Evolution of the Universe," *Nature*, vol. 162, p. 680, 1948.

[8] R. A. Alpher, H. A. Bethe, and G. Gamow, "The Origin of Chemical Elements," *Physical Review*, vol. 73, p. 803, 1948.

[9] G. Gamow, "The Origin of Elements and the Separation of Galaxies," *Physical Review*, vol. 74, p. 505, 1948.

[10] A. S. Eddington, *The Internal Constitution of Stars.* Cambridge University Press, 1926.

[11] H. Bethe, "Energy Production in stars," *Physics Review*, vol. 55, pp. 434–456, 1939.

[12] M. Wiescher, H. Schatz, and A. Champagne, "Reactions with Radioactive Nuclei and Explosive Nucleosynthesis," *Phil. Trans. Royal Soc. Ser.*, vol. A356, p. 2105, 1998.

[13] M. Guidry, "The rapid proton capture process." material presented in the Summer Study of Radioactive Ion Beam Physics held at the Oak Ridge National Laboratory in August,1994.

[14] E. E. Salpeter, "Nuclear Reactions in Stars Without Hydrogen.," *Astrophysical Journal*, vol. 115, pp. 326–328, mar 1952.

[15] E. E. Salpeter, "Nuclear Reactions in Stars. Buildup from Helium," *Physical Review*, vol. 107, pp. 516–525, July 1957.

[16] W. D. Arnett and J. W. Truran, "Carbon-Burning Nucleosynthesis at Constant Temperature," *Astrophysical Journal*, vol. 157, pp. 339–+, July 1969.

[17] W. D. Arnett, "Advanced evolution of massive stars. V - Neon Burning," *Astrophysical Journal*, vol. 193, pp. 169–176, Oct. 1974.

[18] W. D. Arnett, "Hydrostatic Oxygen Burning in Stars. I. Oxygen Stars," *Astrophysical Journal*, vol. 173, pp. 393–+, Apr. 1972.

[19] S. E. Woosley, W. D. Arnett, and D. D. Clayton, "Hydrostatic Oxygen Burning in Stars. II. Oxygen Burning at Balanced Power," *Astrophysical Journal*, vol. 175, pp. 731–+, Aug. 1972.

[20] W. D. Arnett, "Advanced evolution of massive stars. VII - Silicon burning," *Astrophysical Journal*, vol. 35, pp. 145–159, Oct. 1977.

[21] E. M. Burbidge, G. R. Burbidge, W. A. Fowler, and F. Hoyle, "Synthesis of the Elements in Stars," *Reviews of Modern Physics*, vol. 29, pp. 547–650, 1957.

[22] M. S. Smith and K. E. Rehm, "Nuclear Astrophysics Measurements with Radioactive Beams," *Annual Review of Nuclear and Particle Science*, vol. 51, pp. 91–130, 2001.

[23] "TRIUMF-ISAC Gamma-Ray Escape Suppressed Spectrometer (TIGRESS)—Scientific Roadmap 2005," Aug. 2005.

[24] W. R. Leo, *Techniques for Nuclear and Particle Physics Experiments.* Spinger-Verlab Berlin Heidelberg New York, 1987.

[25] A. Ostrowski, S. Cherubini, *et al.*, "CD:A double sided silicon strip detector for radioactive nuclear beam experiments," *Nuclear Instruments and Methods in Physics Research A*, vol. 480, pp. 448–455, 2002.

[26] G. F. Knoll, *Radiation Detection and Measurement.* John Wiley & Sons, 1979.

[27] C. Kittel, *Introduction to Solid State Physics.* John Wiley & Sons, 1967.

[28] D. A. Hutcheon, S. Bishop, *et al.*, "The DRAGON facility for nuclear astrophysics at TRIUMF-ISAC: design, construction and operation," *Nuclear Instruments and Methods in Physics Research A*, vol. 498, pp. 190–210, Feb. 2003.

[29] C. Wrede, A. Hussein, J. G. Rogers, and J. D'Auria, "A double sided silicon strip detector as a DRAGON end detector," *Nuclear Instruments and Methods in Physics Research B*, vol. 204, pp. 619–624, May 2003.

[30] O. T. U. C. Bergmann, H. O. U. Fynbo, "Use of Si strip detectors for low-energy particles in compact geometry," *Nuclear Instruments and Methods in Physics Research A*, vol. 515, pp. 657–664, 2003.

[31] Geant4 Collaboration, S. Agostinelli, J. Allison, *et al.*, "Geant4—a simulation toolkit," *Nuclear Instruments and Methods in Physics Research A*, vol. 506, pp. 250–303, July 2003.

[32] G. Booch, *Object-Oriented Analysis and Design with Applications.* The Benjamin/Cummings Publishing Co. Inc, 1994.

[33] SRIM–The Stopping and Range of Ions in Matter– is a collection of software packages which calculate many features of the transport of ions in matter,http://www.srim.org/.

[34] http://www.srim.org/SRIM/SRIM2003.htm/.

[35] Advanced Measurement Technology, Inc., Oak Ridge, TN 37831-0895 U.S.A.

[36] Micron Semiconductor Ltd., Lancing, BN15 8UN, UK.

[37] GEANT4 home page, http://wwwasd.web.cern.ch/wwwasd/geant4/geant4.html.

[38] J. Liberty and J. Hord, *Teach Yourself ANSI C++ in 21 Days.* Sams Publishing, March 1996.

[39] B. Stroustrup, *The C++ Programming Language.* Addison-Wesley Professional, February 2000.

[40] J. Görres, M. Wiescher, and F.-K. Thielemann, "Bridging the waiting points: The role of two-proton capture reactions in the rp process," *Physical Review C*, vol. 51, pp. 392–400, 1995.

[41] M. Wiescher and H. Schatz, "Impact and Perspectives of Radioactive Beam Experiments for the rp-process," *Nuclear Physics A*, vol. 693, pp. 269–281, oct 2001.

[42] K. Alder and A. Winther, *Coulomb Excitation.* NEW YORK: Academic Press, 1966.

[43] T. Glasmacher, "Coulomb Excitation at Intermediate Energies," *Annual Review of Nuclear and Particle Science*, vol. 48, pp. 1–31, 1998.

[44] D. C. Radford, C. Baktash, J. R. Beene, *et al.*, "Coulomb Excitation of Radioactive ^{132,134,136}Te Beams and the Low B(E2) of ^{136}Te ," *Physics Review Letters*, vol. 88, no. 222501, 2002.

[45] H. Schatz, L. Bildsten, A. Cumming, and M. Wiescher, "The Rapid Proton Process Ashes from Stable Nuclear Burning on an Accreting Neutron Star," *The Astrophysical Journal*, vol. 524, pp. 1014–1029, oct 1999.

[46] H. Schatz, A. Aprahamian, V. Barnard, L. Bildsten, A. Cumming, M. Ouellette, T. Rauscher, F.-K. Thielemann, and M. Wiescher, "End Point of the rp Process on Accreting Neutron Stars," *Physical Review Letters*, vol. 86, pp. 3471–3474, apr 2001.

[47] T. Motobayashi, "Coulomb excitation studies with radioactive nuclear beams," *Journal of Phys. G*, vol. 24, pp. 1569–1574, 1998.